LBL-12058 c.2

Lawrence Berkeley Laboratory
UNIVERSITY OF CALIFORNIA

Materials & Molecular Research Division

MICROSTRUCTURE AND MECHANICAL PROPERTIES OF 0.1C STEEL WITH Nb

Jing-Sheng Gau
(M.S. thesis)

April 1981

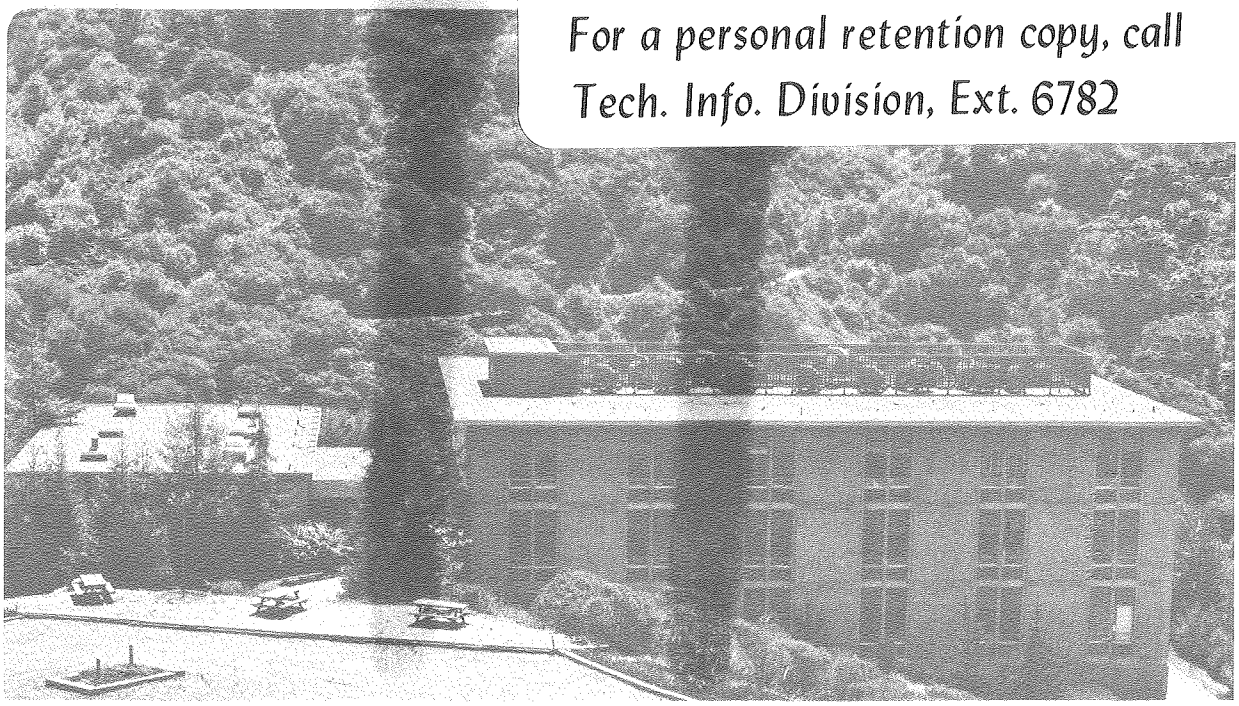

Prepared for the U.S. Department of Energy under Contract W-7405-ENG-48

DISCLAIMER

Microstructure and Mechanical Properties of 0.1C Steel with Nb

Jing-Sheng Gau

Materials and Molecular Research Division

Lawrence Berkeley Laboratory

University of California

Berkeley, CA 94720

M. S. Thesis

April 1981

This work was supported by the Director, Office of Energy Research, Office of Basic Energy Sciences, Division of Materials Sciences of the U.S. Department of Energy under Contract No. W-7405-ENG-48.

1. INTRODUCTION

For a physical metallurgist, especially in the field of alloy design, the problem of research involves synthesis rather than just analysis. To synthesize means to combine the effect of alloy chemistry and processing techniques to optimize the composition and microstructure and hence properties, both economically and favorably.

Mainly due to the energy crisis, interest in the development of so-called dual phase steels during the past decade is well-documented[1-7]. These are steels which have a uniform mixture or composite of ferrite and martensite as the basic constituents. Also, the potential applications of dual phase steels has generated much research activity in this field in recent years.

Using a second phase to improve the properties of an alloy system is not a new idea[8-9], and the processes used to obtain the dual phase structures in the solid state are summarized in Table 1-A. During the past years, great efforts have demonstrated that various processes, as listed in Table 1-B, are available to produce duplex microstructure from plain carbon steels with small additions of alloying elements. Plain carbon steels suffer from poor hardenability; thus the main function of microalloying elements is to improve the hardenability or to provide fine grain size control. However, in order to improve the formability of the dual phase steels which substitute for conventional HSLA steels in the automobile industry, research has been directed toward obtaining "clean" ferrite by choosing appropriate austenite-forming elements[10]. They result in the decrease of dissolved C in ferrite by enhancing the partitioning of carbon between austenite and ferrite and do not produce appreciable solid solution hardening of ferrite. As is known, the main

strengthening comes from the martensite (transformed austenite). Thus a dual phase steel composed of these two important phases which together produce a composite with good strength and ductility is expected to have potential for diverse structural applications (fatigue[11], corrosion, resistance, toughness at low temperatures[12], etc.). Therefore, it is interesting to study the role of ferrite-forming elements[13-15] in the strengthening of dual phase steel as an additional parameter since the ferrite stabilizers are also carbide formers and can be potentially useful in ferrite strengthening.

With a fixed composition, many factors such as annealing temperature, cooling rate, transformation path, etc. govern the final morphology of the metastable martensite. The size, shape, volume fraction, distribution and composition of this primary second phase all affect the mechanical properties. Hence, it is potentially useful to study the effect of the processing variables and to subsequently optimize the processing factors to obtain good properties. Empirically it has been found that the mechanical properties appear to follow a law of mixtures[7]. For example, the general expression for the ultimate tensile strength (σ_c) of dual phase steels approximating to a fiber-reinforced composite model is given by:

$$\sigma_c = \sigma_\alpha (1 - V_m) + \sigma_m V_m$$

where σ_α is the stress in the ferrite at the ultimate tensile strain of martensite, σ_m is the tensile strength of martensite, and $(1-V_m)$ and V_m are their respective volume fractions. Various annealing temperatures will determine the volume fractions of martensite for a particular heat treatment, and the cooling rate following the annealing will determine whether martensite is present or not. In addition, the transformation

path will influence the morphology of duplex microstructures. It is expected these variables are among the most important processing factors.

To summarize, one of the main objectives of the present research is to strengthen the ferrite matrix by enhancing precipitation through the presence of strong carbide-forming elements, Nb and Mo. This is, in light of the conceptual implication of the mixture rule, an attempt to affect the values of σ_α (and possibly σ_m) of the above expression. Meanwhile, the validity of the mixture law, regarding V_m as the decisive factor in the ultimate tensile stress, and σ_α, σ_m being independent will be revealed.

A further objective is to study the effect of processing variables on the mechanical properties and resultant microstructure. The three most important process factors, i.e., annealing temperature, cooling rate and transformation path have been chosen as the variable.

II. EXPERIMENTAL PROCEDURES

A. Materials

1. Selection

The alloy composition used in this study is listed as follows: (wt. pct).

Fe	C	Si	Nb	Mo
Balance	0.1	0.45	0.045	0.1

The Fe/C/Si system which has been well characterized[7] has been selected as a base. The principles of selection for the microalloying elements are as follows:

Carbon (0.1%)

1) the content is kept as low as possible within the limitation of maintaining sufficient hardenability. This is determined roughly from the equilibrium Fe-C diagram: the carbon

content of austenite must be less than 0.3 wt. pct. to result in a dislocated martensite, otherwise the undesirable twinned martensite would deteriorate the toughness[16].

2) For weldability, the carbon content is kept at or below 0.1 wt. pct.

3) These low alloy steels are available. But such a low carbon content is expensive to produce in commercial steel making processes.

Silicon (0.45%)

1) Silicon is known to broaden the (α+γ) two phase range[7].

2) It has a tendency to retard cementite formation and thereby probably also the pearlite formation.

3) In amounts of approximately 2 wt. pct. Si promotes a fine fibrous morphology which results in better toughness[7].

4) Because the industrial application of Fe/2Si/.1C may be hindered by difficulties in galvanizing[13], the amount of Si in this study is reduced. Other microalloyed elements are expected to compensate for the loss of hardenability.

Niobium (0.045%)

1) Niobium is a ferrite-forming element and a strong carbide forming element (NbC).

As reported[17], the maximum amount of Nb that should be soluble in 0.1 pct. C, 0.01 pct. N, austenite at 1250°C is 0.095 wt. pct. The typical commercial niobium addition is about 0.03 wt. pct. For these reasons, the amount of Nb is chosen to be about 0.05 wt. pct. in this research.

2) Niobium is known to retard austenite recrystallization. This would then have the effect of grain refinement in the final ferrite matrix. However, the detailed mechanism which may be either solute

drag effects or precipitate pinning is still in debate[18].

3) Nb provides the system with more hardenability and increases the slope of the A_3 line. That is, by broadening the two phase region, the practical control of the volume fraction of martensite is facilitated.

Molybdenum (0.1%)

1) Molybdenum is also a ferrite forming element and a carbide forming element (hexagonal Mo_2C) in the ferrite matrix. The crystallographic relation[19] of Mo_2C in ferrite has been found to be:

$$(001)_\alpha \;//\; (0001)\; Mo_2C$$

$$(100)_\alpha \;//\; (2\bar{1}\bar{1}0)\; Mo_2C$$

$$[100]_\alpha \;//\; [2\bar{1}\bar{1}0]\; Mo_2C$$

2)Molybdenum provides moderate solid solution strengthening and increases the slope of the A_3 line.

2. Preparation

The experimental alloy Fe/.1C/.45Si/.045Nb/.1Mo was supplied by the Climax Molybdenum Company. The material was received in the form of round plates. It was first homogenized in argon at 1100°C for 24 hours, forged and then rolled into a plate of 3/8" x 3" cross section. Oversized tensile flat blanks were machined with the rolling direction parallel to the tensile axis.

B. Heat Treatment

The hot rolled oversized tensile specimens were heat treated in a vertical tube (3" I.D.) furnace under an argon atmosphere. Various cooling rates such as in air cooling, forced air cooling, water quenching and ice brine quenching were carried out. The corresponding cooling curves were recorded by a type K (chromel-slumel) thermocouple at the

center of each specimen with a strip chart recorder. This data is shown in Fig. 1.

The heat treatment scheme for the first part of the study, the optimization of the processing variables of annealing temperature and cooling rate for simple (direct) annealing, is schematically represented in Fig. 2.

The various heat treatment processes used to vary the morphologies are plotted in the schematic representation of Fig. 3. The design ideas follow:

The direct process referred to as Process I produces a morphology which is dependent on the initial, as-received microstructure of the alloy. It has the advantage of simple processing with lower production cost.

The continuous annealing heat treatment (Process II) is an industrial practice which is designed to simulate the hot-rolled condition. The advantage is obvious--a continuous process saves energy otherwise to reheat the material.

The intermediate quench heat treatment (Process III) was devised to fully exploit the characteristics of an initial martensite structure prior to annealing. This provides another opportunity to study the kinetics of intercritical annealing.

C. Mechanical Testing

After heat treatment, the slightly oversized tensile blanks were machined to one inch gauge length tensile specimens, following the ASTM specification E8-69 shown in Fig. 4.

Uniaxial tensile testing was done at room temperature in an Instron machine with a full scale load of 1500kg and a 0.5cm/min crosshead speed.

The total elongation was measured by the difference in the one-inch gauge before and after the test and was used to check the result obtained from the directly machine-plotted stress-strain curves. The yield strengths were determined by the 0.2% offset method. Other mechanical properties were determined from the curves recorded by the test machine's chart recorder.

D. Metallography

1. Optical Metallography

Optical metallography was performed to determine the microstructure and morphology.

Specimens were cut from heat-treated materials either mounted in Bakelite or in Kold-mount, ground successively on silicon carbide papers from 180 to 600 grit, and polished with 1μ diamond paste on a felt cloth lubricated with kerosene.

An etchant solution of 2% Nital was used to reveal the duplex constituents. The samples were then examined on a Zeiss Ultraphot V Microscope, and their volume fractions were estimated by the line intersection method.

2. Scanning Electron Microscopy

An ARM-150 scanning electron microscope (SEM) operated at 20 kV was used for the fractography study. It was also used to study the slip line distributions in tensile specimens (which were polished following the procedures for optical metallography before the test). Specimens used for optical metallography were reexamined at higher magnification under SEM to obtain better resolution and depth of field. To obtain better contrast, a thin gold film was evaporated onto each specimen.

An energy dispersive analysis of x-rays (EDAX) unit attached to the

scanning electron microscope was used to analyse the chemical composition semiquantitatively.

3. Transmission Electron Microscopy (TEM)

Thin foils for TEM studies were obtained by cutting 20 mils (500μm) slices from the heat treated material using the slow feed, flood cooled abrasive cutter. These slices were then chemically thinned down to less than 5 mils in a solution of 4% HF in H_2O_2. After 3mm diameter discs were spark cut from these slices, they were carefully ground on 600 grit paper down to 1-2 mils. These discs were cleaned in acetone and finally electropolished in a twin-jet electro-polishing apparatus at room temperature with an electrolytic solution of 75gm Cr_2O_3 + 400ml CH_3COOH + 21 ml distilled H_2O. The voltage was kept at 40V with the current at 55-60mA. These thin foils so obtained were kept in ethyl alcohol for later use. The foils were examined in either a JEM 7A or Philips 301 electron microscope operated at 100kV. The chemical identification of inclusions was carried out by EDAX using the Philips 400 analytical electron microscope.

E. X-ray Analysis

X-ray analysis was used to determine the existence of the amount of retained austenite in the alloy studied[20-21]. Specimens cut from the heat treated material were prepared by first mechanical grinding 10mils off the surfaces. This was done to remove the surface layer which may be decarburized or nonrepresentative of the bulk. Grinding was followed by standard polishing to ensure a flat and reproducible surface. Finally, 0.02 inch was chemically removed from the surface of the specimens with a solution of 4% HF in H_2O_2 to eliminate any possible strain-induced surface effect due to plastic deformation.

The G.E. Diano x-ray diffractometer with filtered M.Kα radiation was used to examine the specimens after various heat treatments. The scan angle$^{(20)}$ covered was from 20° to 40° which included the prominent $(220)_\gamma$, $(311)_\gamma$ reflections of austenite and $(200)_\alpha$, reflections of martensite.

III. RESULT AND DISCUSSION

A. Microstructure

The final structure is a function of processing variables and depends predominantly on the initial microstructure prior to heat treatment.

Fig. 5 shows the morphologies of the material before heat treatment (Fig. 5-B); the full martensitic structure quenched from the γ phase (Fig. 5-A); and the mixed ferritic and pearlitic microstructure after air cooling from the γ phase (Fig. 5-C). These photographs show that the microstructure is quite different in each case.

The resultant microstructures of the first part of this study--the effect of annealing temperature and cooling rate can be seen in Fig. 6. All air cooling and forced air cooling processes would result in a microstructure composed primarily of ferrite and pearlite. Furthermore, by varying the transformation path, the resultant duplex microstructures are shown in Fig. 7.

From the equilibrium Fe-C phase diagram, it is evident that when an iron-carbon alloy is held at a temperature between A_1 and A_3, the alloy will separate into a mixture of γ phase with a high carbon content and α phase with a low carbon content. The formation of either the ferrite or the austenite by nucleation and growth governs the final microstructure and morphology. For the direct process (Fig. 3-A), the

What is more interesting is that when the cooling rate following the two phase intercritical annealing is high enough to ensure that the austenite transforms to martensite, the resultant microstructure is an aggregate of duplex ferrite and martensite. Fig. 12 shows the microstructure consisting of globular martensite dispersed in the ferrite matrix. Nevertheless, the attached semiquantitative EDAX spectrums failed to provide data on any composition difference.

Fig. 13 is an example of a TEM image of the ferrite present between martensite packets. The most important feature in this image is the high density of dislocations associated with the region adjacent to martensite. Also, in this region, precipitation is less pronounced. Referring to Fig. 8, it is expected that precipitation occurring during annealing and/or cooling would play an important role in the final morphology and resultant properties. With the carbide-forming elements, the precipitation reaction in this study shows some general behavior as revealed in Figs. 14 and 15. A boundary precipitate free zone (PFZ) and dislocations free from precipitation as shown in Fig. 15 can both be understood on the basis that the boundary and the dislocations serve as vacancy and solute sinks.

Comparative studies[24-26] of V, Nb and Ti additions have been reported. These HSLA dual phase steels (except the V) after intercritical annealing and air cooling gave properties corresponding to those of normalized or hot rolled HSLA steels. This is confirmed in this investigation even with the addition of Mo, and with higher cooling rates. The reason for this, i.e., the fact that a slow cooling rate cannot produce the desired duplex microstructure is because the amount of the elements Nb and Mo present does not increase the hardenability sufficiently.

The Nb and Mo, to a large extent, will be precipitated before and during annealing. As pointed out before, even niobium carbide inclusions were found (Fig. 20). It is instructive to study the partitioning behavior of the microalloying elements. However, attempts to analyze the partitioning of Nb and Mo elements have failed because of their limited amounts in relation to the EDAX detectability limit of the Philips EM 400.

As seen in Figs. 9 and 10, precipitation following the heat treatments with slow cooling (cooling rates $\leq$ 10°C/sec) either from γ phase or the two phase region, is not pronounced. Most precipitation events would occur during the intercritical annealing. Figs. 14 and 16 show the precipitate observed after 800°C and 850°C, water quenching which would yield 20% and 40% martensite respectively. Knowing that the intercritical annealing is not an equilibrium event, the volume fraction of martensite is a function of annealing temperature, time, cooling rate and transformation path. Hence, the density of precipitation due to the excess vacancy concentration after quenching to room temperature and the partition of carbon and microalloyed elements varies in each case. In this study, there are two variants of plate-like precipitates visible for the g = [100] diffraction condition in Fig. 14. This results in a precipitation density of about $3 \times 10^{16}/cm^3$ by examining the extinction fringe[27]. For the 850°C water quenching treatment with the assumption of 800Å foil thickness statistically[28], there would be a density of $5 \times 10^{15}/cm^3$ as estimated in Fig. 16. The density of precipitates is an important factor in explaining the dependence of strength vs. volume fraction of martensite.

To obtain more reliable data of the density of precipitates as a function of annealing temperature which in turn fixed the volume fraction

of martensite, the convergent beam technique in TEM should be used to obtain a more accurate estimation of the foil thickness and the statistics be taken into account.

Furthermore, Figs. 17 and 18 show the morphology of precipitates observed after various transformation paths. The precipitation occurs more predominantly in Process II (continuous annealing) than in Process III (intermediate annealing). In reality, the precipitation path varies for each process. For continuous annealing, precipitation might already exist in starting condition, e.g., the undissolved inclusion, precipitation before the annealing, during the intercritical annealing and/or during cooling after the annealing. These parameters are not easy to measure quantitatively[21] neither can the kinetics of precipitation and the separation of the quantities that has precipitated prior to the γ to α transformation and during cooling be determined. The transformation behavior can be better understood with the aid of a R.P.T. diagram such as that shown in Fig. 8, if known. This sort of diagram could be a basis for understanding the process-structure-property for hot-working conditions such as controlled rolling to obtain duplex structures. Based on the discussion of Process I (direct annealing), most precipitation events occur during the annealing. For the intermediate annealing process, the precipitation involves various stages of tempering during reheating from the initial supersaturated carbon content of martensite.

Generally, the strong carbide-forming elements Nb and Mo produce fine plate-like precipitates lying on {100} in the ferrite matrix. This was done by the trace analysis of Fig. 14. These alloy-carbide and vacancy-cluster precipitates are expected to be an important strengthening mechanism.

Inclusions have been found to exist in this material. Fig. 19 shows that the dislocations interacted with inclusions after the heat treatment of air cooling from 945°C γ phase annealing. Fig. 20 shows the identification of these inclusions by analytical microscopy as being niobium-carbides from the EDAX spectrum in TEM. These inclusions might probably originate from the material preparations.

In this investigation, no retained austenite was found either by x-ray analysis or by TEM examinations. The retained austenite could help improve the work hardening rate[6,10] and other mechanical properties[30], and its amounts could be up to the order of 10% volume fraction in dual phase steels with the addition of austenite stabilizers. However, with the ferrite-forming elements Nb and Mo, the material is expected to have a higher Ms temperature. In addition, the heating history is not fast enough to cause severe segregation of microalloyed elements, although niobium inclusions exist. Therefore, it is concluded that the amount of retained austenite present in the DFM aggregates must be less than 1%.

Precipitation during the γ-α transformation is very sensitive to the holding time and the cooling rate. It is possible that further decomposition of austenite after intercritical annealing would result in the so-called transformed ferrite between the martensite and the retained ferrite[31,32].

This can be identified by the double etching technique[33]. In this material, even with the high cooling rate of agitated ice brine quenching, the existence of transformed ferrite was found[34]. The partitioning behavior is an important factor in studying the precipitation. As pointed out before, an attempt to analyse such behavior was

unsuccessful. The inhomogeneity of composition is plainly evident in Fig. 21, where microtwins were found in the martensite. The diffusion of the substitutional elements is so slow at the intercritical annealing temperature that equilibrium partition is not achieved[31]. However, carbon diffuses an order of magnitude faster and this approaches its equilibrium concentration. Nevertheless, the local equilibrium concentration is determined by the concentration of substitutional alloying elements present. Consequently, a high carbon concentration can exist even within a single austenite grain. This accounts for the occurrence of microtwins in the martensite, as it is known that twinning probability in martensite increases with % carbon (beyond about 0.4%).

The resultant microstructures for the processing variables of cooling rates and annealing temperatures are summarized in Table II, and that of transformation path is given in Table III.

B. Mechanical Properties

1. General Considerations

The mechanical properties are summarized in Table IV and V; typical stress-strain curves from tensile tests are shown in Figs. 22 and 23. Some important differences and characteristic features of the dual phase steel are immediately evident. The discontinuous yielding characteristic of conventional ferrite and pearlite microstructures has been eliminated by the formation of the dual-phase structure, i.e., ferrite and martensite. The removal of this discontinuous yielding is probably due to the increased population of the glissile dislocations in the ferrite induced by the martensitic transformation which prevents the drag effect of solute atoms. The high density of mobile dislocations can be seen in Fig. 13 and Fig. 18. The continuous yielding of dual phase steels has the

advantage of eliminating the need for temper rolling or other operations during metal forming.

Other characteristics of duplex ferrite and martensite microstructure are also obvious, e.g., a high work hardening rate and a high tensile strength to yield strength ratio. The high work hardening rate, which would yield more uniform strain distribution, is due to the increase with the plastic stress of the effective size of the martensite as an obstacle to moving dislocations during plastic deformation. The higher ratio of tensile to yield strength is because of the low value of yield strength and high tensile strength. Since there are lots of mobile dislocations in the ferrite region, the yield strength is relatively low. The high tensile strength results from the load-carrying martensite.

However, the analysis of the true stress-strain behavior yields information that the work hardening index, n value (defined later) is not a constant (see Table IV). This implies that many processes are involved in the plastic deformation. To date, many models[34-38] have been developed to describe the plastic deformation of two phase systems, but none has completely succeeded, even though the plastic deformation of single crystals[39] is well understood in terms of the basic deformation mechanisms of slip and twinning. Furthermore, an approximation of the relation between the polycrystal deformation and single crystal deformation has been developed[40] by taking into account the average orientation factor (the reciprocal of the Schmid factor). The most common empirical approach to modeling the flow of behavior is a power expression of the true stress and true strain in the form[35,39] as follows:

$$\sigma = K\varepsilon^n$$

where n is the work-hardening index which reflects the ability of the material to resist necking. The value of n is numerically equal to the true strain at U.T.S.; i.e., $n = \varepsilon u$, an important criterion in the formability[41]. As expected, a high work hardening rate (a high n value) is desirable in the automobile industry because material with higher work hardening rate exhibits a more uniform strain distribution. That the n values were not constant implies that many processes occurred successively during the plastic deformation and the weight of each mechanism was so complicated that so far only a qualitative description was available. In addition to the contribution of the precipitated particles, the aggregated strong martensites would be further obstacles to the moving dislocations. Hence a high work hardening rate was established.

2. Effect of Annealing Temperature

Annealing at 800°C and 850°C followed by water quenching yields about 20% and 40% volume fraction of martensite respectively.

The comparison of mechanical properties is shown in Fig. 24 where there is a tendency for strength to depend upon the volume fraction of martensite. Using the mixture rule:

$$\sigma_c = \sigma_\alpha(1 - V_m) + \sigma_m V_m \quad ,$$

the volume fraction of martensite is the critical factor governing the strength. This is also the conclusion of the work by Davies[42] who claimed that the strength is independent of the composition of martensite, being influenced only by the ferrite grain size and the volume fraction of martensite. In this investigation, the U. T. S. shows no significant dependence upon the volume fraction of martensite. This might be due to the pronounced precipitation in the ferrite (Table II)

and the carbon content in martensite[43] which in turn determines the strength of martensite, this decreasing with increasing volume fraction of martensite. The apparent failure of the mixture rule results from the fact that it does not take into account the size, shape and distribution of the martensite product nor does it account for the degree of internal connectivity.

In dual phase steels, the elongation during a tensile test is terminated by ductile fracture at the hard, brittle islands of martensite responsible for the initiation of cracking (see later section). Rashid[24] has shown that the total elongation is greatly reduced when the volume fraction of martensite is increased over 20%. In this study, the above conclusion was found not to apply. The ability of a crack to propagate to eventual failure is a function of the size, shape of martensite and the ductility of ferrite. Therefore, even with the same shape and size of martensite, the volume fraction is not the only variable to be considered.

3. Effect of Cooling Rate

The variations of strengths as a function of cooling rate are plotted in Fig. 25. From this, both the strength and the U.T.S./Y.S. ratio increase with increasing cooling rate.

Fig. 26 shows the slip line distributions[44] in the tensile heat specimens. As can be seen, the deformation started from within the soft ferrite matrix. Some cross slip was also observed. The slip line was inclined about 50° to the tensile axis. Basically, the idea of DFM is analogous to that for composite materials, viz., the incorporation of the inherently strong martensite as a load-carrying constituent in a soft ferrite matrix[7]. The yield strength is determined by the flow stress of the ferrite, and not affected by the strength of the martensite.

Following Pickering and Gladman's approach[45], the yield strength σ_y can be expressed in the following equation

$$\sigma_y = \sigma_o + \Sigma K_i \gamma_i + \Sigma k_j C_j + k_y d^{-1/2} + P_{ij}$$

where σ is the Peierls lattice stress of the ferrite matrix, the second term represents the solid solution strengthening of microalloyed components, the third term arises from the precipitate particles, the next term is the grain size effect from the Hall-Petch equation, d the grain diameter, and the final term P_{ij} the residual stress due to the strain field introduced by the martensitic transformation which would affect the value of σ_o at a finite region, the larger the effect, the higher the cooling rate.

In this investigation, the DFM aggregates have high yield strengths. This arises from the fact that Mo and Nb are ferrite stabilizers. They do not decrease carbon solubility in ferrite via the partitioning of C. Also Nb and Mo cause solid solution hardening and precipitation hardening in the soft matrix. Therefore, we expect to have higher yield strength than that of a typical DFM steel used for the automobile industry. The strength of martensite, which governs the ultimate tensile strength, increases with increasing cooling rate because of the larger residual stresses and the higher supersaturation of carbon due to the near elimination of diffusion events.

In Table II, a tempering[46] heat treatment intended to prevent quench cracking during agitated ice-brine quenching (the highest cooling rate of about 1000°C/sec in this study), immediately altered the characteristics of dual phase steels. Ductility was improved but the low work hardening rate and the discontinuous yielding behavior reappeared.

This primarily arose from the disappearance of martensite which characterized the dual phase system. Therefore, tempering to render required ductility to fully martensitic steels, is not necessary in the applications of dual phase steels. In view of fundamental research, the tempering behavior would be of interest.

Finally, after choosing the cooling rate as the primary process factor for a given annealing temperature, one can combine this with the effect of the alloy content expressed in terms of equivalent content by extensively varying the alloy content. Therefore, the alloy content-cooling rate-mechanical properties diagram[10] as a schematic representation can be drawn (see Fig. 27). The advantage of this diagram is obvious. The formation of the dual phase microstructure could be predicted for any combination of alloy content and cooling rate and therefore the optimum production condition for dual phase steels could be realized.

4. Effect of Different Transformation Paths

By changing the transformation path, the variations in the final mechanical properties reflect the differences in the morphology of the resultant martensite product.

The highest U.T.S. (115ksi) is obtained by continuous annealing (Process II). This results in a morphology of large irregular-shaped chunk martensite in the ferrite matrix. Contrary to the prediction of the Hall-Petch equation, the high strength is due to the large size of the martensite islands; however, the poor ductility is due to the increase in the dislocation mean free path. This increases the stress concentrations at the ends of slip bands where dislocations are forced to pile up against barriers, in this case, the strong martensite phase. Instead, the fibrous morphology of martensite product in the intermediate

annealing (Process IV) has the best ductility (~20%). This can be understood on the basis of the efficiency of load transfer. With the lath martensite shape, load transfer is most efficient because the transfer of load occurs by shear action along particle/matrix interfaces[7,47]. For a given volume fraction, more interfacial area is available in the case of a fibrous morphology.

C. Fractography

Materials exhibit many different types of fracture depending on the material itself, and its microstructure, heat treatment and testing conditions.

In this investigation, all the material was tested in the uniaxial tensile test with slow cross-head speed, and exhibited the cup and cone fracture surfaces indicative of ductile fracture. A typical example is shown in Fig. 28. Ductile fracture in tension usually starts by necking at the point of plastic instability. This is followed by the formation of voids and finally coalescence to fracture. The preferred sites for void formation are those where the strain compatibility during deformation is difficult, that is, near the second phase and the inclusion. Fig. 29 shows some inclusions which couldn't be identified by EDAX in SEM. As discussed before, the inclusion is probably niobium carbide.

Although the true strain to fracture decreases rapidly with increasing fraction of second phase particles[48,49], this is not the case when the second phase is aggregated instead of dispersed. As shown in Table VI the fracture stresses for the 20% and 40% martensite are not very different. Furthermore, the shape of the second phase can have an influence on ductile fracture. When it is fibrous as in the case of Process III, cracking is much more difficult and the ductility

is therefore improved as discussed before.

Conclusions

From this investigation of the characterization of the microstructure and mechanical properties in a Fe/.01C/0.45Si/0.045Nb/0.1Mo steel, the following conclusions can be drawn:

(1) No retained austenite is found.

(2) All air cooling and forced air cooling processes result in a microstructure mainly comprised of ferrite and pearlite with a corresponding tendency for undesirable discontinuous yielding.

(3) The strength and the U.T.S./Y.S. ratio increases with increasing cooling rate.

(4) Following direct intercritical annealing, the U.T.S. has no significant dependence upon the volume fraction of martensite. Instead, a decreased relationship was found.

(5) The volume fraction of the martensite is a function of cooling rate, annealing temperature, holding time and also the transformation path.

(6) The ferrite-forming elements Nb and Mo produce fine plate-like precipitates lying on the {100} plane in the ferrite matrix.

(7) For the 800°C annealing followed by water quenching, the density of precipitates is about $3 \times 10^6/cm^3$.

(8) By changing the transformation path, the highest tensile strength (115ksi) is produced, however, the best ductility (20%) is obtained from the intermediate intercritically annealing heat treatment.

(9) Referring to Fig. 30, the dual phase heat treatment in this material results in better mechanical properties in comparison to commercial HSLA re-bar steels.

Acknowledgements

I extend my appreciation and gratitude to Professor Gareth Thomas for his guidance, stimulating encouragement and support throughout the course of this study. Helpful discussions with A. Nakagawa and N. J. Kim in the alloy design group and Dr. J. Y. Koo are gratefully acknowledged. I wish to thank L. Rabenberg and Dr. J. J. Rayment for their criticism. Thanks are also due to Professors A. Evans and J. W. Morris, Jr. for reviewing this manuscript.

The assistance of the technical support staff of the Materials and Molecular Research Division of the Lawrence Berkeley Laboratory is recognized. Thanks are due in particular to John Holthuis, Ken Gaugler, Don Krieger and Weyland Wong. The Climax Molybdenum Company kindly supplied the material in this investigation. I would also like to thank Kathy Brusse and Madeline Moore for typing this manuscript.

I am indebted to my family and friends for their encouragement and love, especially the constant support from my elder brother, Jing-Ming.

This work was supported by the Director, Office of Energy Research, Office of Basic Energy Sciences, Division of Materials Science of the U. S. Department of Energy under Contract No. W-7405-ENG-48.

Table 1-A

Processes that produce a second phase in solid state

1. Eutectoid reaction
2. Sloping-solvus precipitation
3. Spinodal decomposition
4. Ordering transformation
5. Two phase region annealing
6. Powder metallurgy

Table 1-B

Processes available to produce dual phase low carbon steels

1. As hot-rolled condition
2. Intercritically annealed condition
3. Gamma phase annealed condition
4. Batch-annealed condition
5. Continuous annealing and processing

Table II. Summarization of final microstructure

Heat Treatment	Matrix	Second Phase	Precipitation in ferrite
800°C air cooling	retained ferrite	pearlite	comparatively clear
800°C FAC	retained ferrite	pearlite	low density of precipitates
800° WQ	retained and transformed ferrite	20% martensite	high density of precipitates $\sim 3 \times 10^{16}/cm^3$
800°C IQ	retained and transformed ferrite	< 20% martensite	$> 3 \times 10^{16}/cm^3$
850°C WQ	retained and transformed ferrite	40% martensite	$\sim 5 \times 10^{15}/cm^3$

Table III. Transformation path effect on the final microstructure

	Heat Treatment	Morphology of Martensite	Precipitation density in matrix
I.	Direct Annealing	Globular	$\sim 10^{16}/cm^3$
II.	Continuous Annealing	Irregular-shaped chunk	$\sim 10^{16}/cm^3$
III.	Intermediate Annealing	Acicular	$\sim 10^{15}/cm^3$

Table IV. Mechanical Testing Data

Annealing Temperature	Cooling Media	U.T.S. (ksi)	Y.S. (ksi)	ε_T (%)	ε_U (%)	Y.S./U.T.S.	Yielding Phenomenon
945°C	Air	59	44	24	24	0.75	Yes
	Forced Air	63	45	35	28	0.71	Yes
850°C	Air	59	44	35	28	0.75	Yes
	Forced Air	61	45	36	28	0.74	Yes
	Water	101	64	17	11	0.63	No
800°C	Air	62	47	36	29	0.76	Yes
	Forced Air	62	48	36	29	0.77	Yes
	Water	106	70	15	10	0.66	No
	Ice Brine	114	74	15	9	0.65	No
	Ice Brine + Tempering	74	56	28	22	0.76	Yes

Table V. Process path effect on the mechanical properties

Heat Treatment Process	n	U.T.S. (ksi)	Y.S. (ksi)	ε_T (%)	ε_U (%)	Y.S / U.T.S.
Direct Intercritical -Annealing	0.53 ↓ 0.30 ↓ 0.28	106	70	15	11	0.66
Continuous Intercritical -Annealing	0.25 ↓ 0.15	115	75	13	9	0.65
Step Intercritical -Annealing	0.13 ↓ 0.21	105	81	20	15	0.77

References

1. Microalloying 75, Proceedings, Union Carbide Corporation, Washington, D. C. 1977.
2. Production and Properties of Vanadium Dual Phase Steel and Cold Pressing Steels in the Automobile Industry. Proceedings of a seminar in Berlin, Vanadium International Technical Committee, October 1978.
3. Formable HSLA and Dual-Phase Steels, A. T. Davenport, ed., AIME, New York, N. Y. 1979.
4. Structure and Properties of Dual-Phase Steels, R. A. Kot and J. W. Morris, eds., AIME, New York, N. Y. 1979.
5. Fundamentals of Dual Phase Steel, AIME, 1981 Symposium, Chicago, February 1981.
6. T. Furukawa, Metal Progress (1979), December, p. 36.
7. J. Y. Koo and G. Thomas, Structure and Properties of Dual-Phase Steels, R. A. Kot and J. W. Morris, eds., AIME, New York, N. Y. 1979; Met. Trans. 8A (1977) 525; Met. Trans. 11A (1980) 852.
8. The Effect of Second Phase Particles on the Mechanical Properties, Iron and Steel Institute, 1971.
9. R. F. Decker, Met. Trans. 4, 2495 (1973).
10. T. Furukawa, H. Morikawa, H. Takechi, and K. Koyama in Structure and Properties of Dual-Phase Steels, R. A. Kot and J. W. Morris, eds., AIME, New York, N. Y. 1979, p. 281.
11. J. Wasynczuk, M. S. Thesis, University of California, Berkeley, 1981, in print.
12. N. J. Kim, Ph. D. Thesis, University of California, Berkeley, 1981, in print.
13. T. J. O'Neill, Jr., M. S. Thesis, University of California, Berkeley, (1979), LBL-9047.

14. A. Nakagawa, M. S. Thesis, University of California, Berkeley, 1981, in print, LBL-12044.

15. P. K. Costello, M. S. Thesis, University of California, Berkeley, 1979, LBL-8628.

16. G. Thomas, Battelle Conference on Fundamental Aspects of Structural Alloy Design, 1979, LBL-4175.

17. H. Nordberg and B. Aronsson, JISI 206, 1263 (1968).

18. S. S. Hansen, J. B. Vander Sande and Morris Cohen, Met. Trans. 11A, 387 (1980).

19. F. G. Berry and R. W. K. Honeycombe, Met. Trans. 1, 3279 (1970).

20. B. D. Cullity, Elements of X-Ray Diffraction, p. 391-396. Addison-Wesley Publishing Company, Inc. (1972).

21. R. L. Miller, Trans. A. S. M. 57, 892 (1964).

22. M. R. Plichta and H. I. Aaronson, Met. Trans. 5, 2611 (1974).

23. M. J. Young, M. S. Thesis, University of California, Berkeley, 1977, LBL-6620.

24. M. S. Rashid, GMR-1044, February 1976, General Motors Company Research Laboratory.

25. J. W. Morrow, G. Tither and R. M. Buck, L-176-182, March 1978, Climax Molybdenum Company Research Laboratory.

26. R. Lagneborg, in Production and Properties of Vanadium Dual Phase Steel and Cold Pressing Steels in the Automobile Industry. Proceedings of a seminar in Berlin, Vanadium International Technical Committee, October 1978.

27. P. Hirsch, A. Howie, R. B. Nicholson, D. W. Pashley and M. J. Whelan, Electron Microscopy of Thin Crystal (1977), p. 511 Butterworth & Co., (Publishers) Ltd., London.

28. R. Hoel, private communication.

29. G. Begin and R. Simoneau in Microalloying 75, Proceedings, Union Carbide Corporation, Washington, D. C. 1977, p. 85.

30. G. Thomas, Met. Trans. 9A, 439 (1978).

31. W. S. Owen, Met. Tech. 1, January 1980.

32. M. D. Geib, David K. Matlock and G. Krauss, Met. Trans. 11A, 1683 (1980).

33. R. D. Lawson, D. K. Matlock and G. Krauss, Metallography 13, 71 (1980).

34. J. S. Gau, research in progress.

35. L. F. Ramos, D. K. Matlock and G. Krauss, Met. Trans. 10A, 259 (1979).

36. B. Karlsson and B. O. Sundstrom, Mat. Sci. & Eng. 16, 161 (1974).

37. M. F. Ashby, in Strengthening Methods in Crystals, A. Kelley and R. B. Nicholson (eds), Elsevier, London, 1971, p. 137.

38. M. F. Ashby, Phil. Mag. 14, 1157 (1966).

39. G. E. Deiter, Mechanical Metallurgy, McGraw Hill, 1976, p. 210.

40. U. F. Kocks, Met. Trans. 1, 1121 (1970).

41. F. B. Pickering, in Hardenability Concepts with Applications to Steel, eds. D. V. Doane, J. S. Kirkaldy, 1978, p. 8.

42. R. G. Davies, Met. Trans. 9A, 41, 451, 671 (1978).

43. E. Bain and H. W. Paxton, Alloying Elements in Steels, 2nd ed., ASM, 1961, p. 37.

44. G. Thomas, Transmission Electron Microscopy of Metals, p. 205, 1962.

45. R. W. K. Honeycombe, Met. Trans. 7A, 915 (1976).

46. R. E. Reed-Hill, Physical Metallurgy Principles, D. Van Nostrand and Co., 1973, p. 733.

47. A. Kelley, in Advances in Composite Materials, ed. G. Piatti, Applied Science Publishers Ltd., London, 1978, p. 113.

48. B. Edelson and W. Baldwin, Trans. Amer. Soc. Met. 55, 230 (1962).

49. T. Gladman, B. Holmes and L. D. McIvor, in The Effect of Second Phase Particles on the Mechanical Properties, Iron and Steel Institute, p. 78, 1971.

Figure Legends

Fig. 1. The cooling curves correspond to the cooling media used in this study. For the water quenching, the curve lies between oil and ice-brine quenching.

Fig. 2. Schematic representation of heat treatment conducted in this study.

Fig. 3. Schematic representation of the various heat treatment processes to study the effect of the transformation path.

Fig. 4. Sketch of a flat tensile specimen.

Fig. 5. Optical micrography of the alloy

(A) full martensite microstructure

(B) microstructure before heat treatment

(C) microstructure after air cooling from γ phase

Fig. 6. Optical micrography of direct intercritical annealing followed by different cooling media (A) 850°C forced air cooling; (B) 800°C air cooling; (C) 850°C water quenching and (D) 800°C water quenching.

Fig. 7. Optical micrographs of the duplex microstructure following the various transformation paths as indicated.

Fig. 8. Schematic representation of the recrystallization-precipitation combined with the continuous cooling diagram.

Fig. 9. TEM micrographs showing the pearlite structure found in the foil air-cooled from γ phase.

Fig. 10. TEM micrographs showing the clean ferrite in the 850°C forced air cooling foil. Some inclusions and dislocations are present.

Fig. 11. TEM micrographs showing the precipitates in ferrite in the 800°C forced air cooling foil.

Fig. 12. SEM micrograph showing duplex microstructures; however, the attached x-ray spectrum fails to tell the composition difference.

Fig. 13. TEM micrographs showing the dislocations present in regions adjacent to the martensite/ferrite interfaces.

Fig. 14. TEM micrograph showing the precipitation-free zone in the ferrite matrix.

Fig. 15. TEM micrograph showing the dislocations free from precipitates.

Fig. 16. TEM micrograph showing the precipitates in the 850°C water quenching foils.

Fig. 17. TEM micrographs showing the precipitates in the ferrite matrix of the continuous intercritical annealing heat treatment.

Fig. 18. TEM micrographs showing the precipitates in the ferrite matrix of the intermediate intercritical annealing heat treatment.

Fig. 19. TEM micrograph showing dislocation climbing over the inclusions in the foil under the heat treatment of air cooling after 945°C annealing.

Fig. 20. TEM micrograph showing that by the use of EDAX system, the inclusions present were identified as niobium carbides.

Fig. 21. TEM micrographs showing the microtwinned martensite (A) bright field; (B) dark field in the 800°C water quench.

Fig. 22. Engineering stress-strain curves for the direct intercritical annealing for various conditions as indicated.

Fig. 23. Engineering stress-strain curves corresponding to the various transformation paths as indicated.

Fig. 24. Plot of the strengths vs. ductility at various volume fractions of martensite.

Fig. 25. Plot of the yield and tensile strengths as a function of cooling rates.

Fig. 26. SEM micrographs showing the slip line distributions at various tensile strains. The left column specimens without etching; the right with etching to show duplex microstructure.

Fig. 27. The schematic representation of the alloy content-cooling rate-mechanical properties diagram.

Fig. 28. SEM micrographs showing the typical cup-and-cone fracture surface in the dual phase steel.

Fig. 29. SEM micrograph of fracture surface with attached x-ray spectrum which fails to identify the inclusions.

Fig. 30. This figure illustrates a comparison of strength vs. total elongation between the commercially available HSLA steels and the DFM alloy in this study.

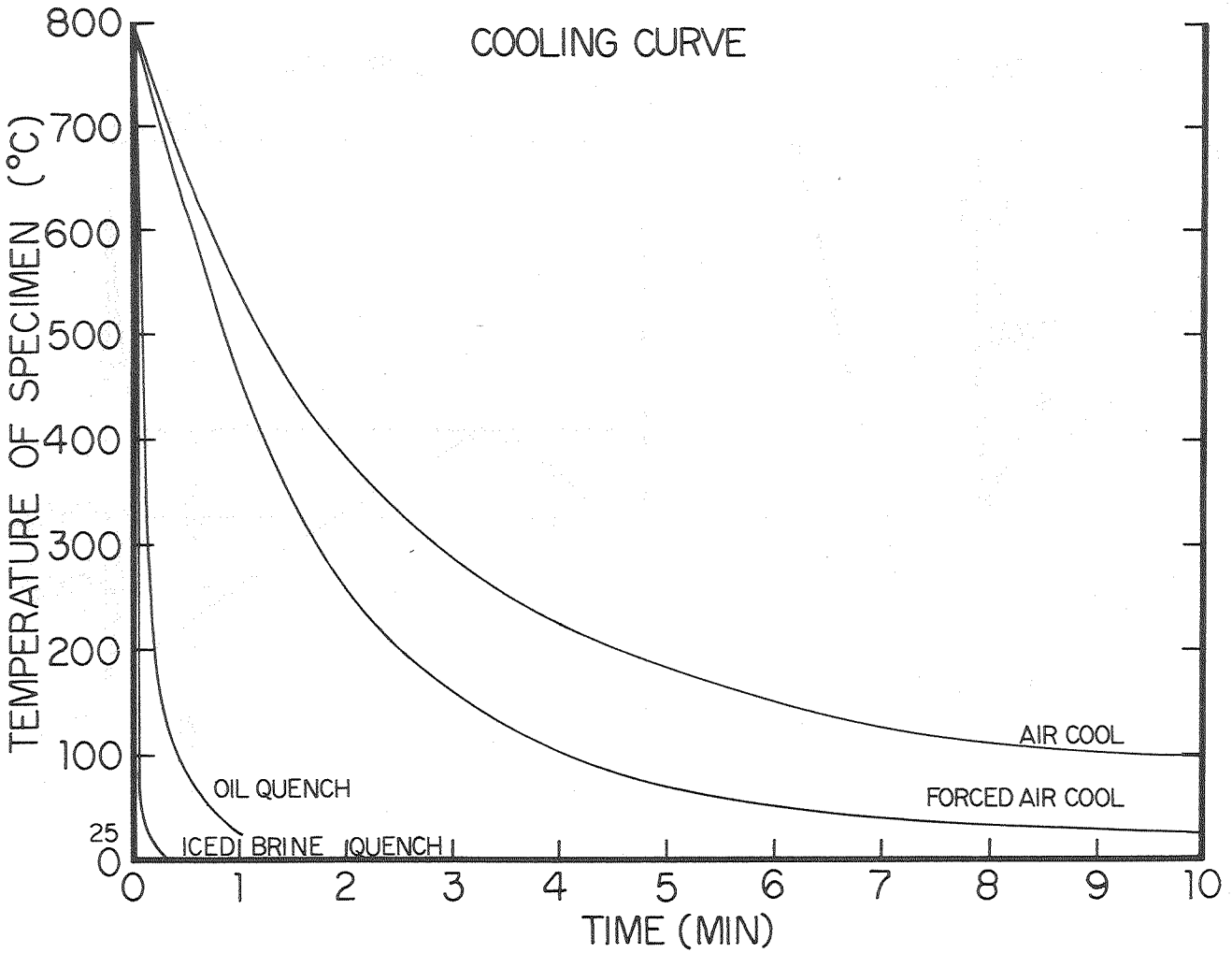

Fig. 1

XBL 8011-7413

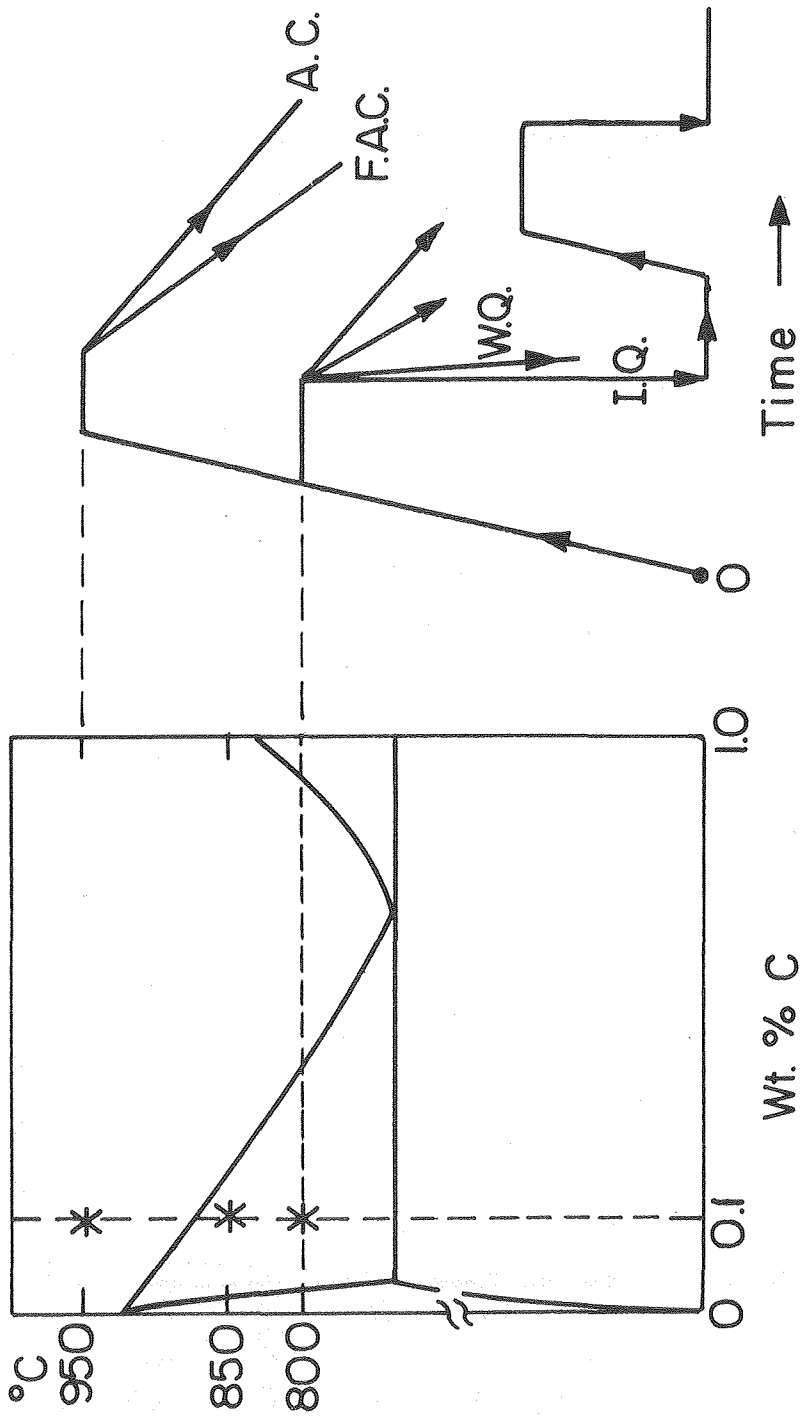

Fig. 2

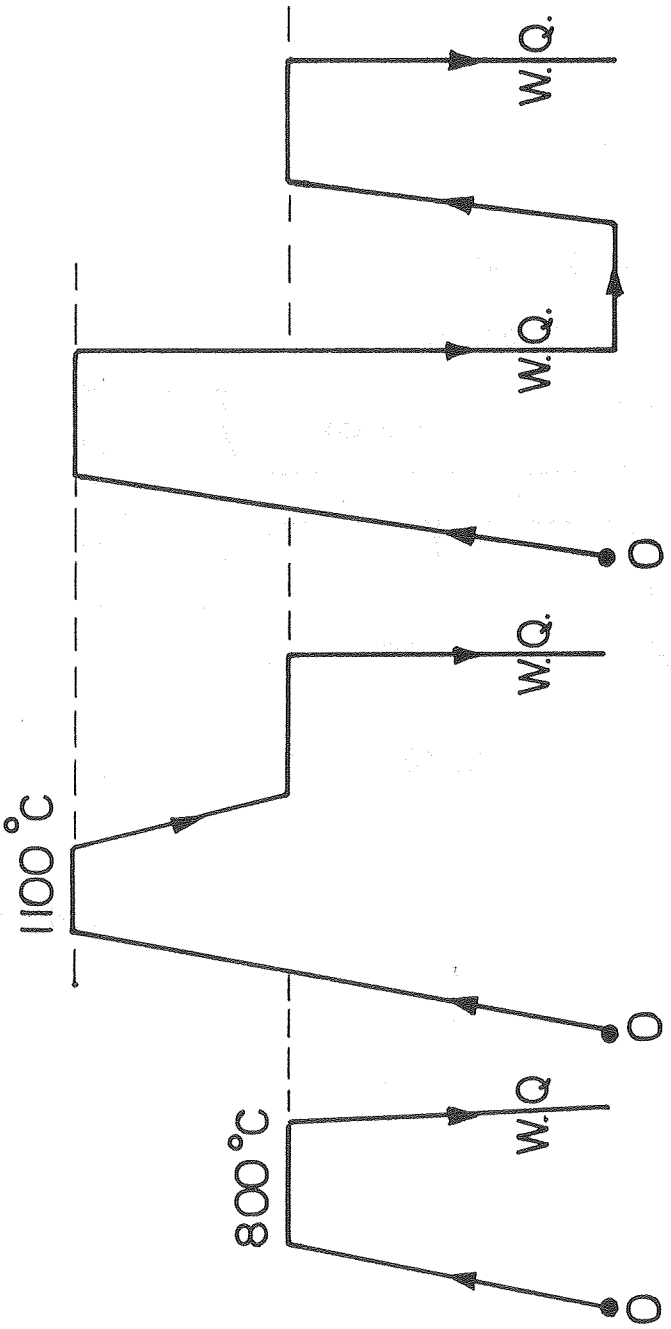

XBL8010-6189

Fig. 3

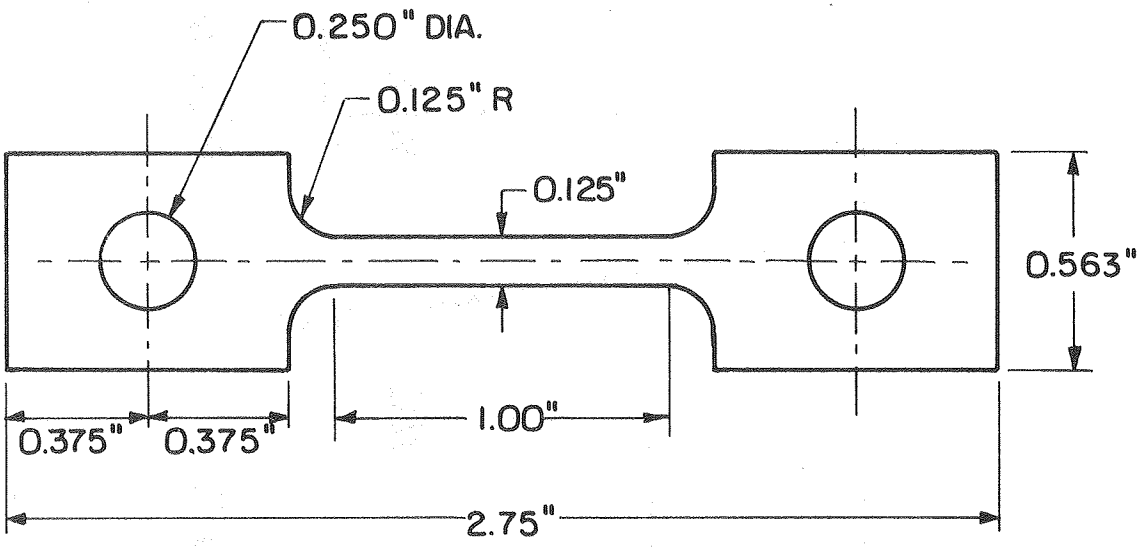

Fig. 4

XBL737-6444

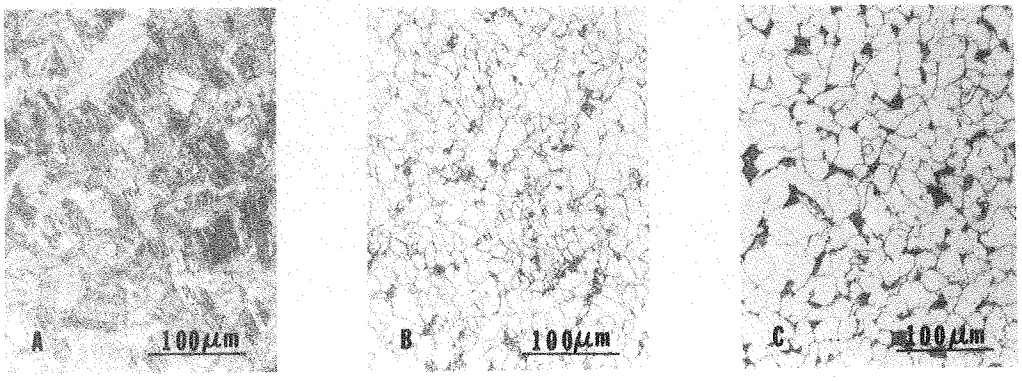

Full Martensite Microstructure

Before H.T. Microstructure

γ-phase Air Cooling Microstructure

XBB 800-14029

Fig. 5

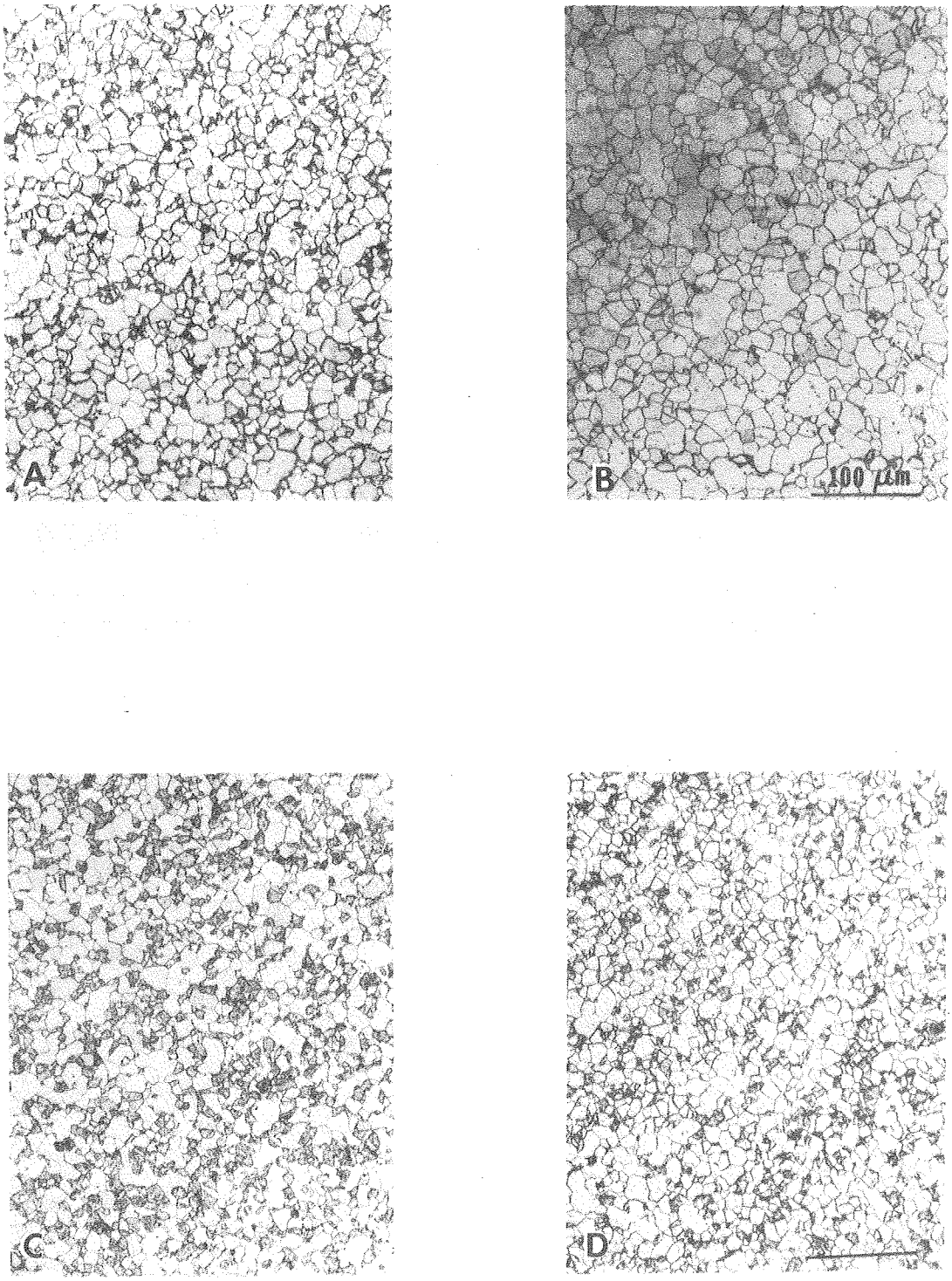

XBB 800-11949

Fig. 6

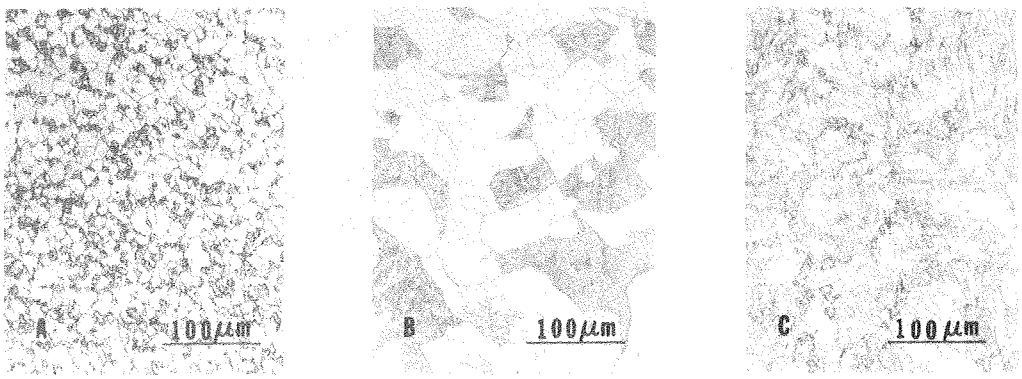

Process I
Intercritical Annealing

Process II
Intercritical Annealing

Process III
Intercritical Annealing

XBB 800-14028

Fig. 7

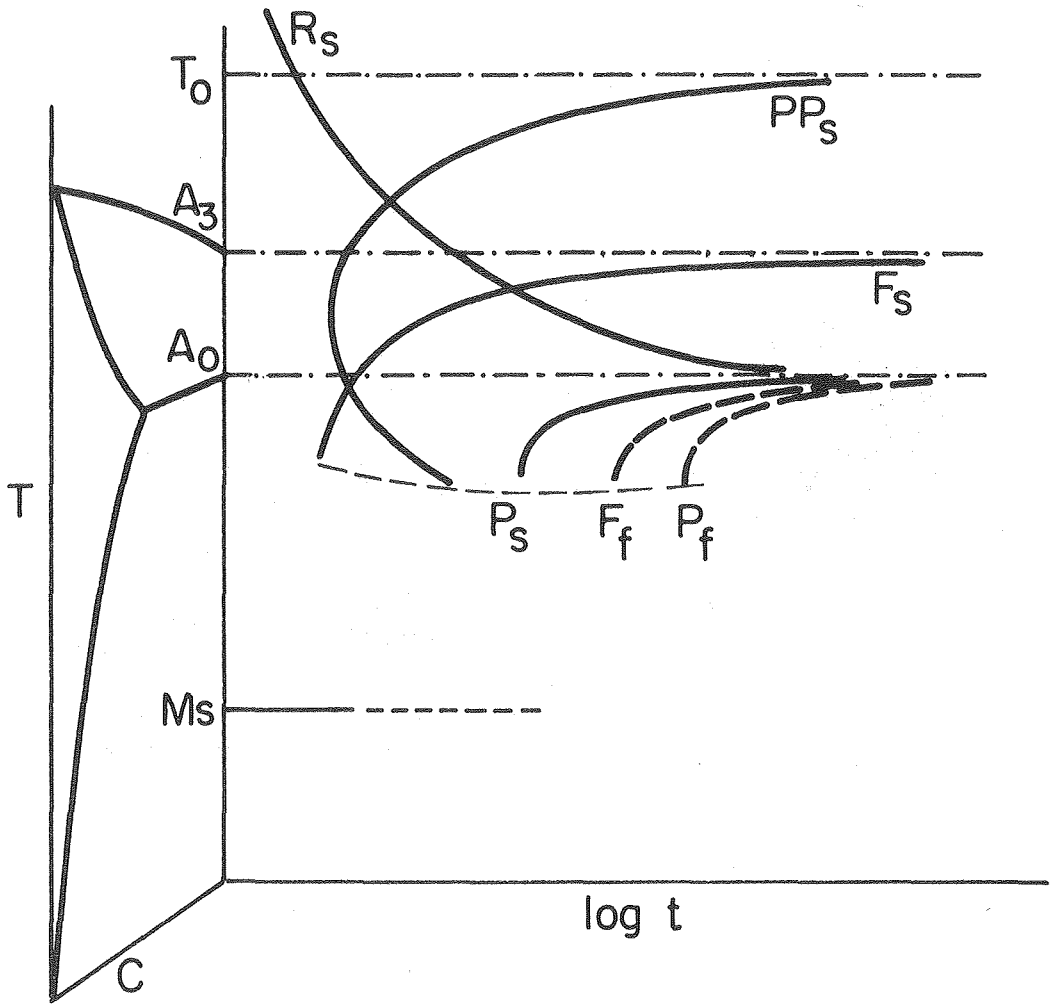

T_O Precipitate solubility temperature

R_S Recrystallization start curve

PP_S Precipitation start curve

$F_{S,f}$ Ferrite start (F_S) and finish (F_f) curves

$P_{S,f}$ Pearlite start (P_S) and finish (P_f) curves

Fig. 8

XBL 8010-6190

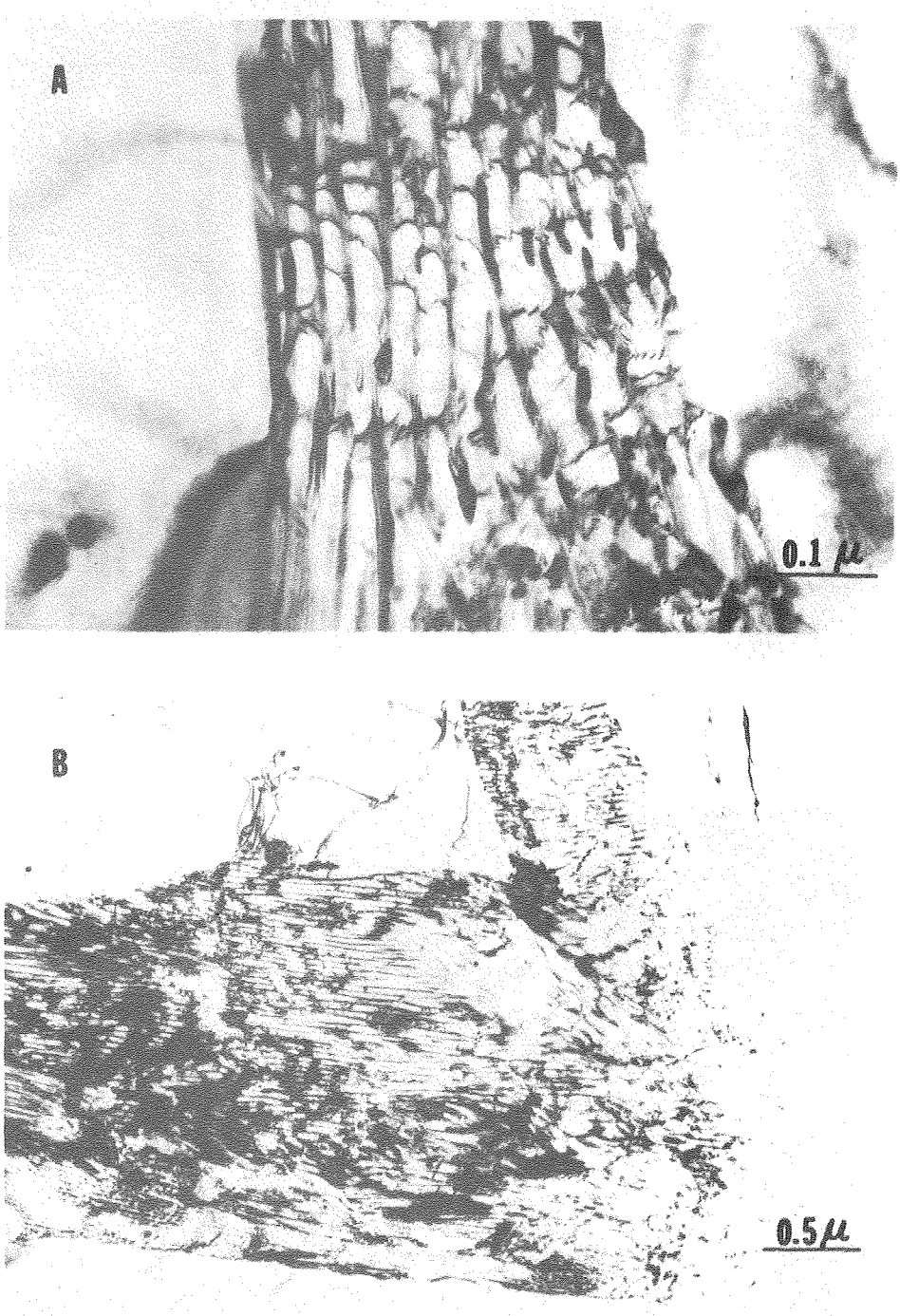

XBB 800-14032

Fig. 9

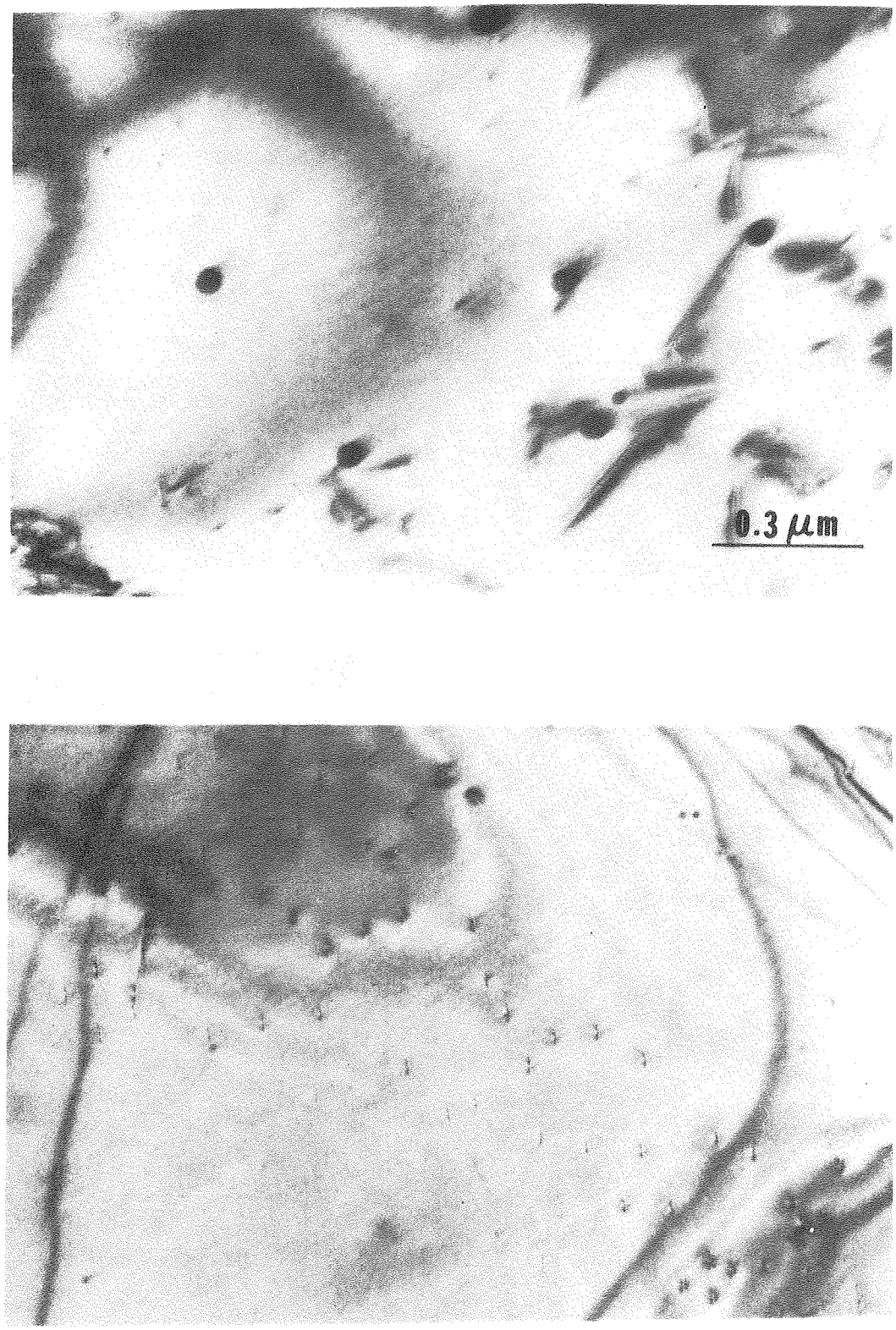

XBB 800-11959

Fig. 10

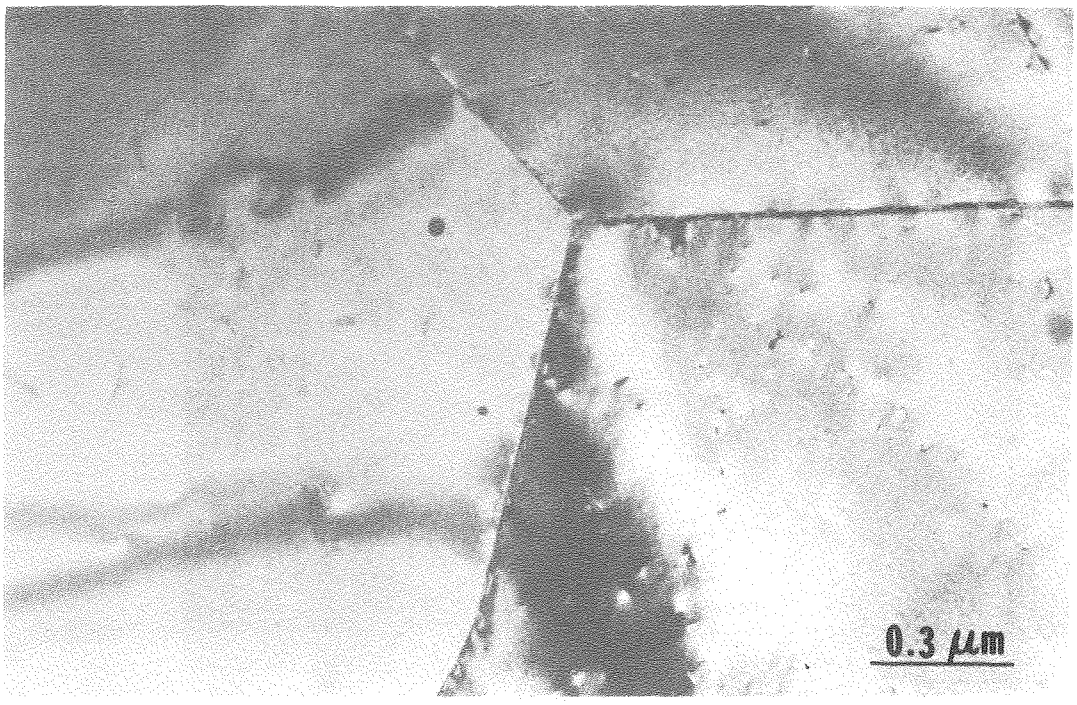

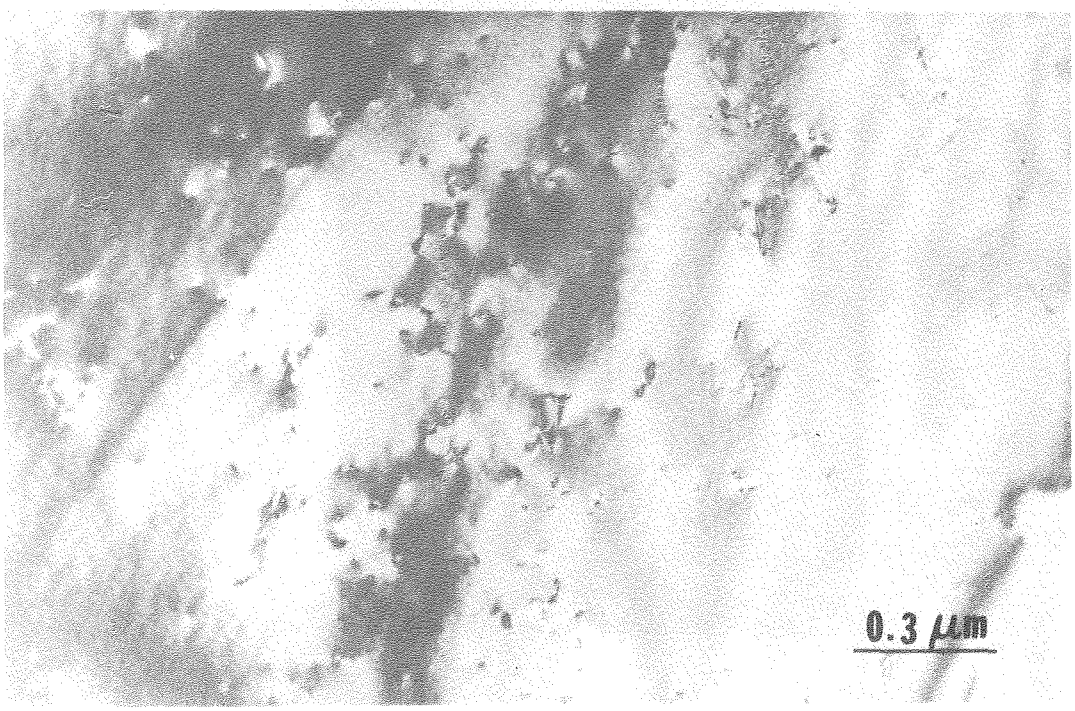

XBB 800-11957A

Fig. 11

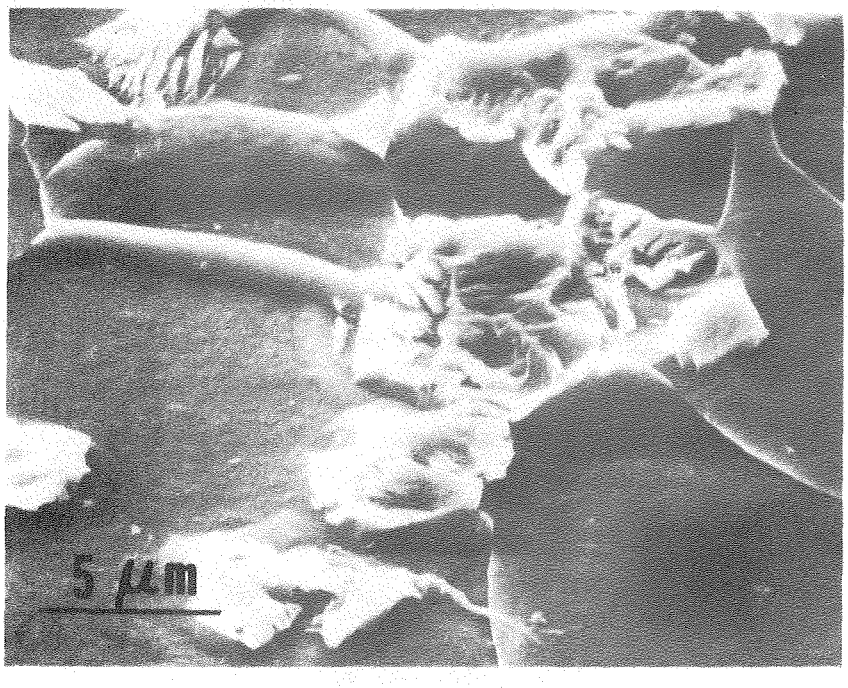

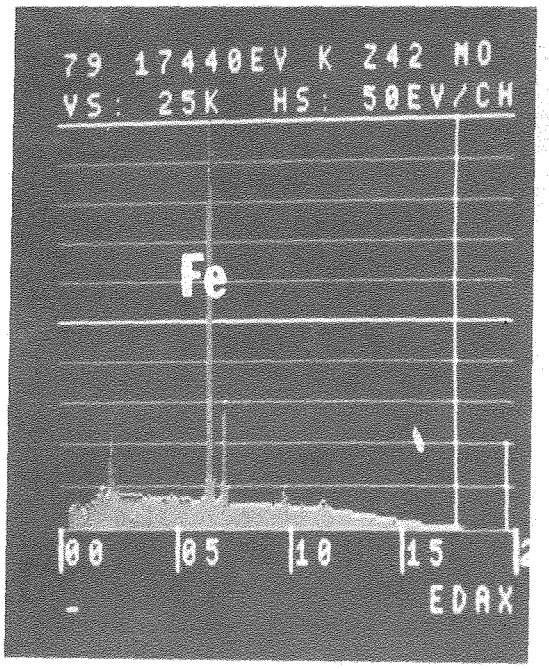

XBB 800-14038

Fig. 12

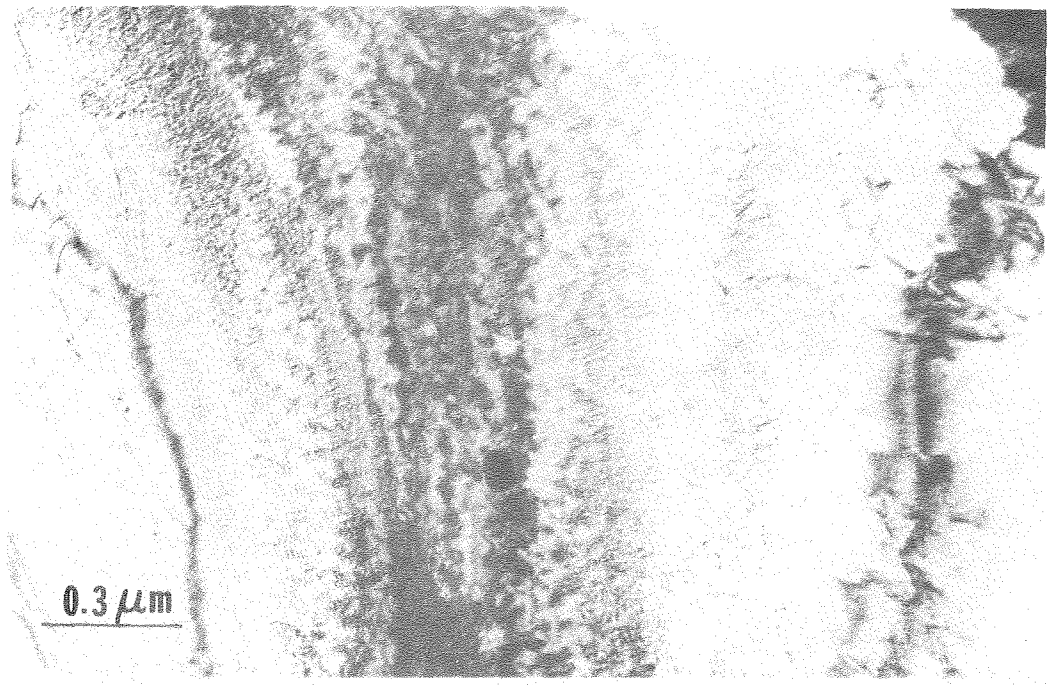

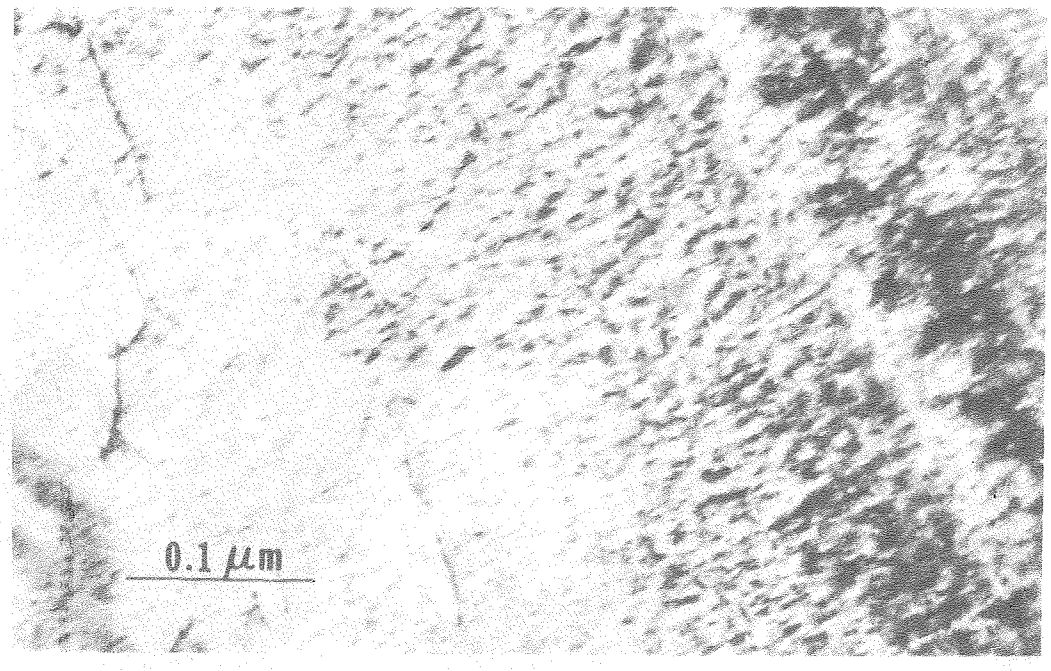

XBB 800-11951

Fig. 13

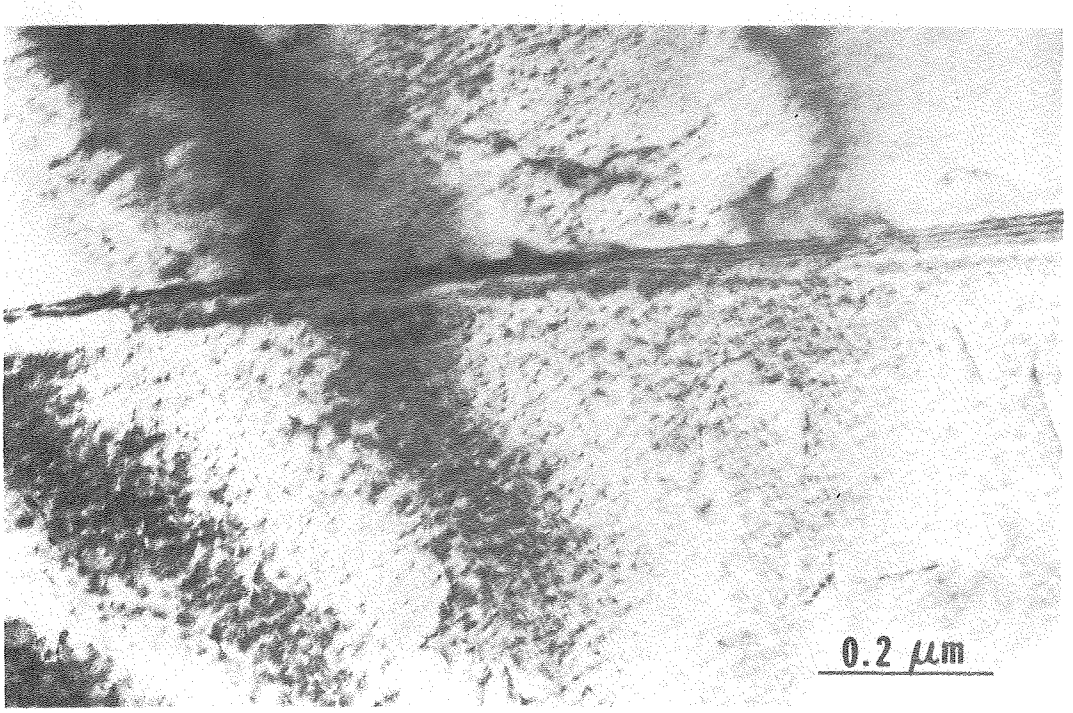

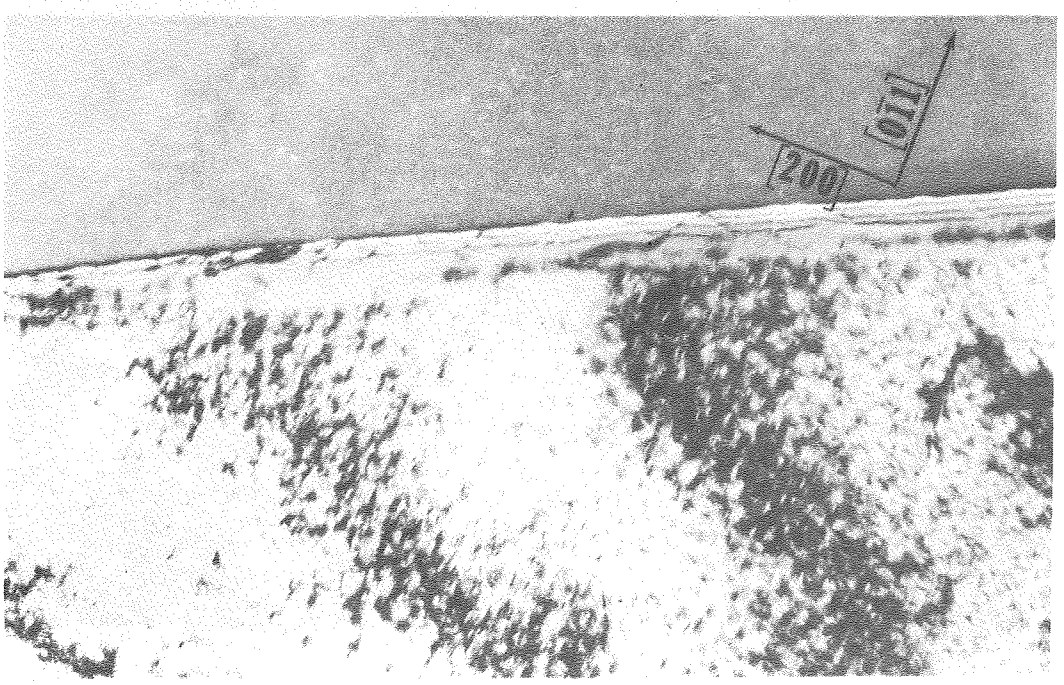

XBB 800-11952

Fig. 14

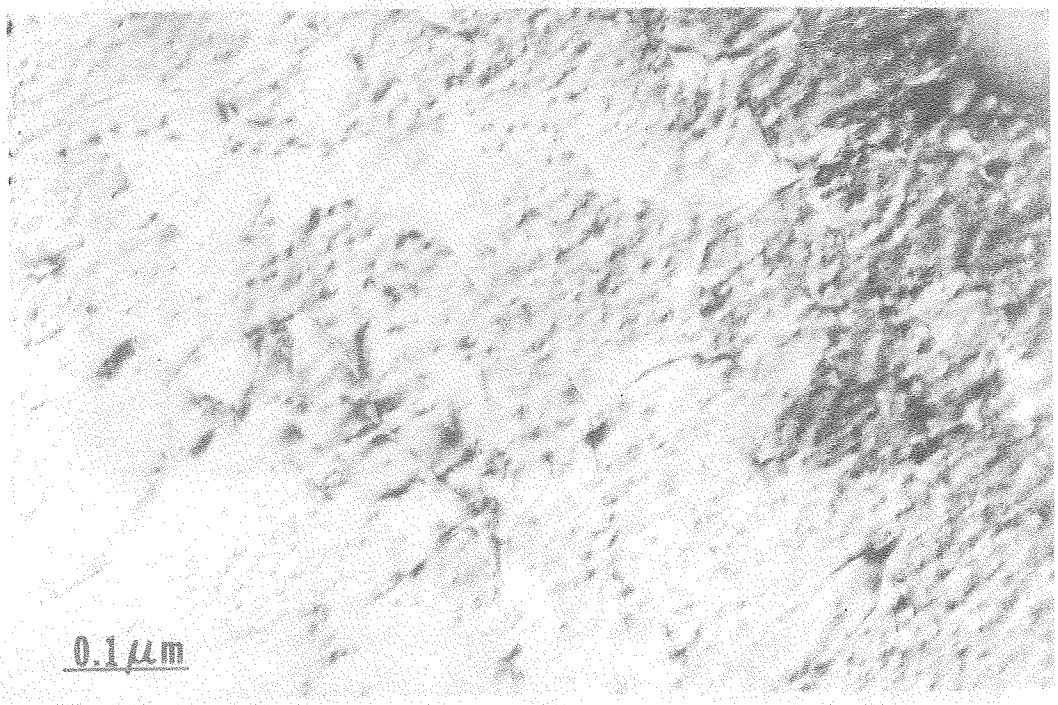

XBB 800-11947

Fig. 15

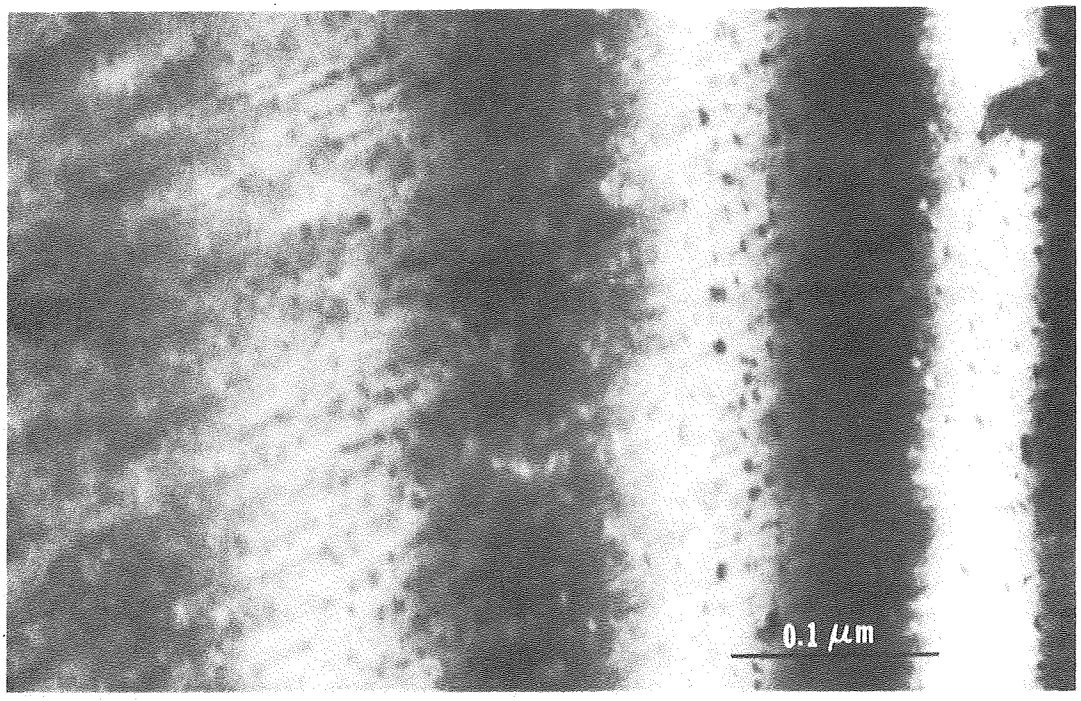

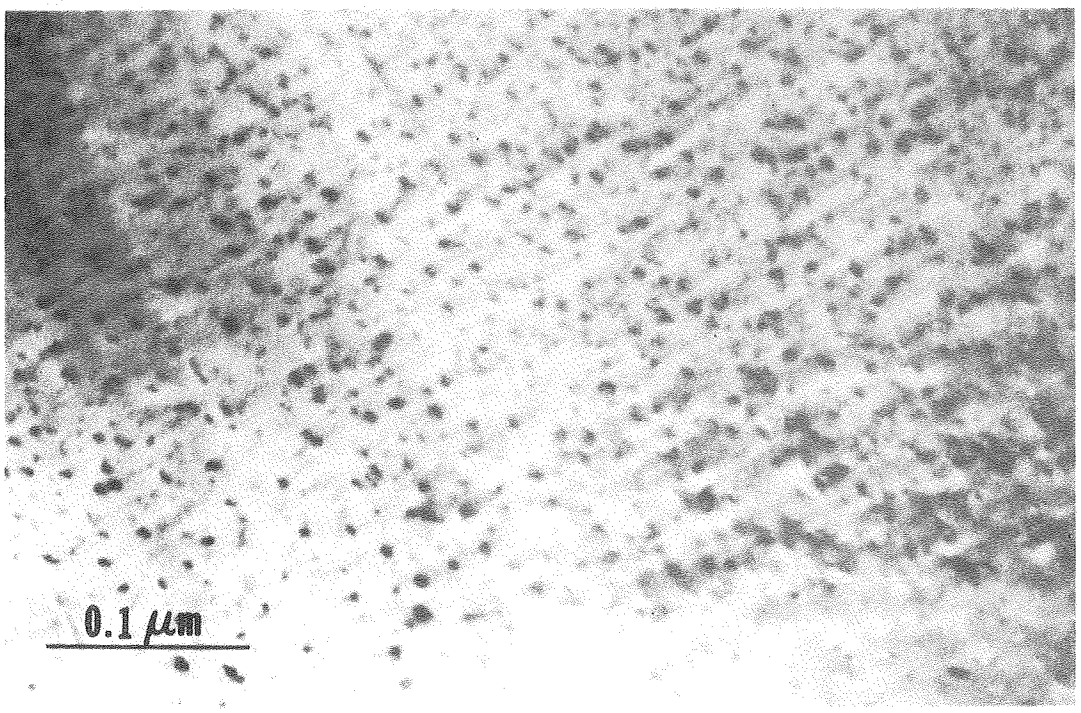

XBB 800-11961

Fig. 16

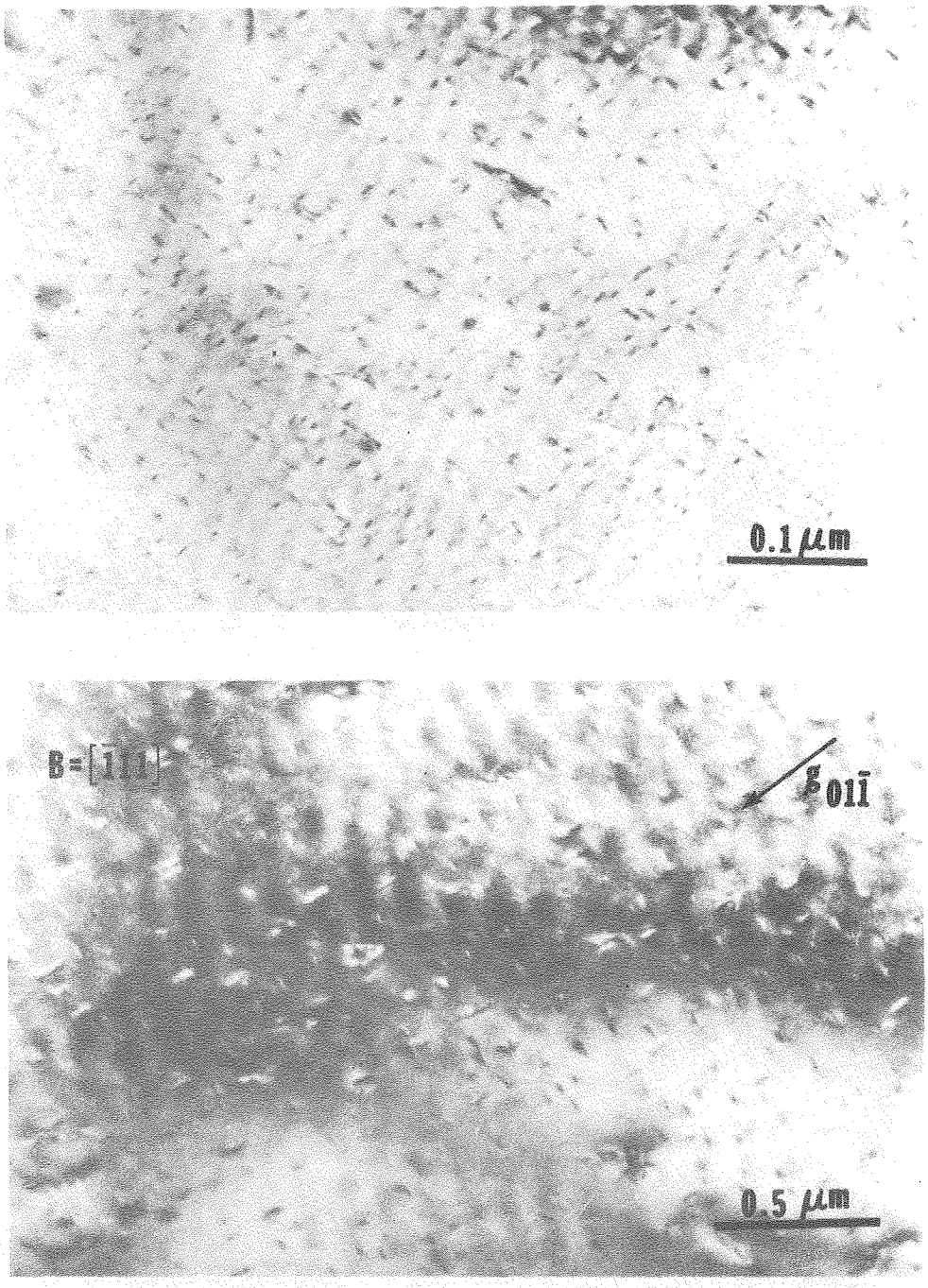

XBB 800-14031

Fig. 17

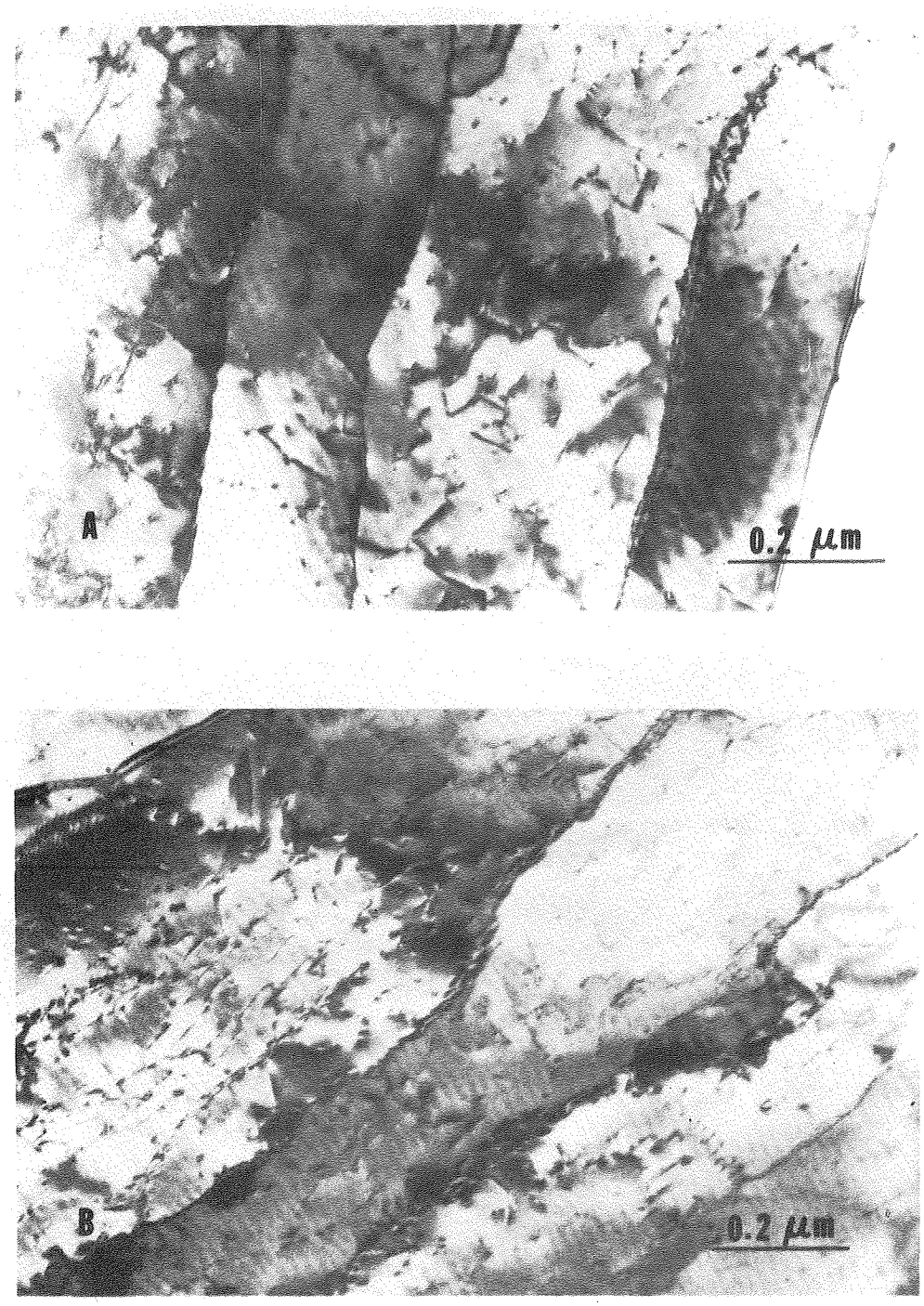

XBB 800-14033

Fig. 18

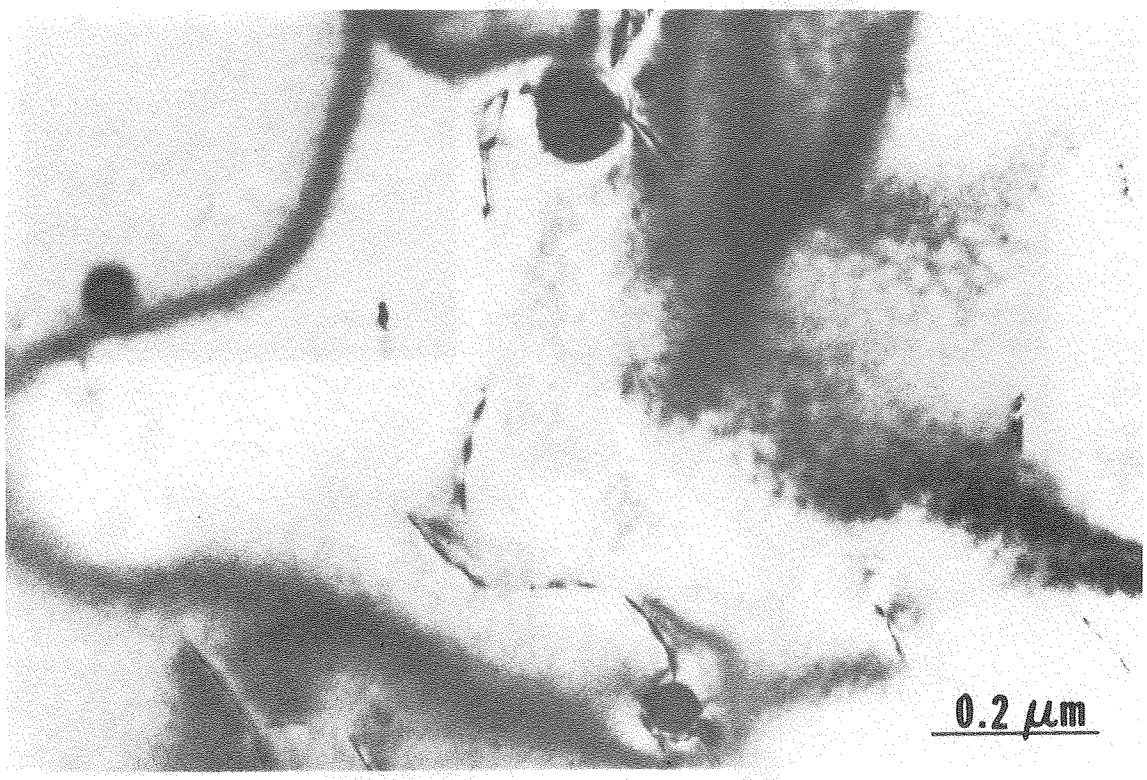

XBB 800-11953

Fig. 19

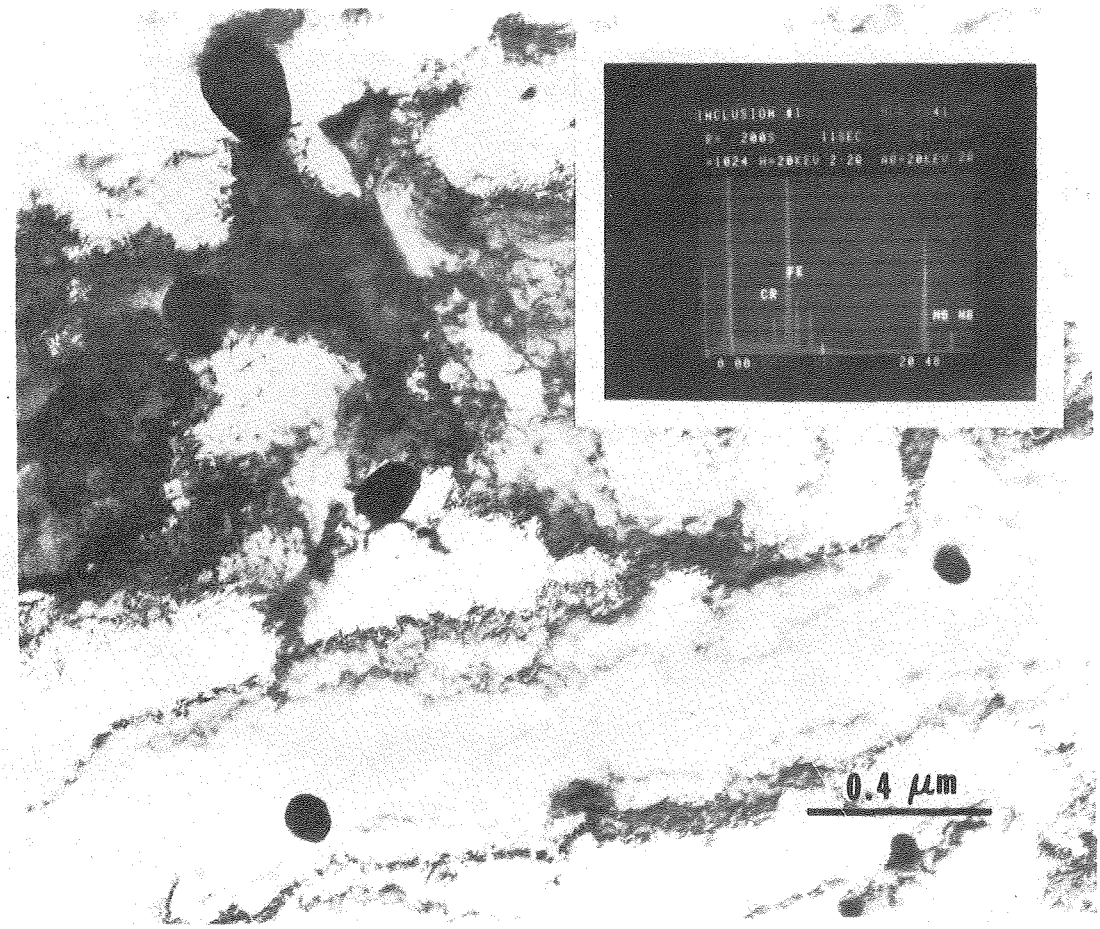

XBB 800-14034

Fig. 20

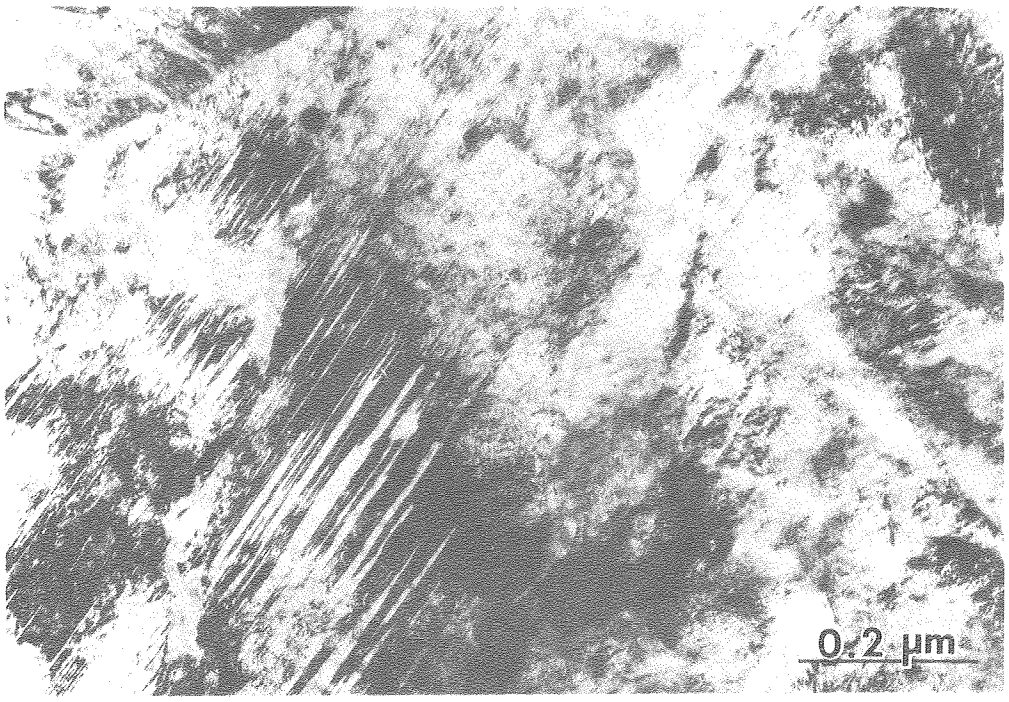

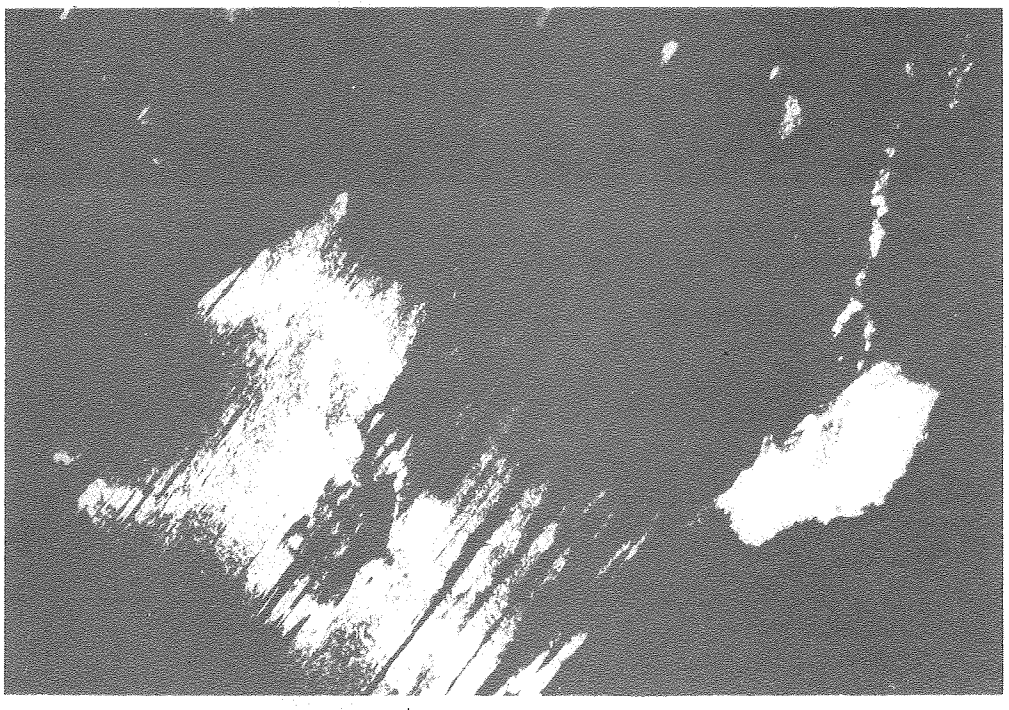

XBB 800-11960

Fig. 21

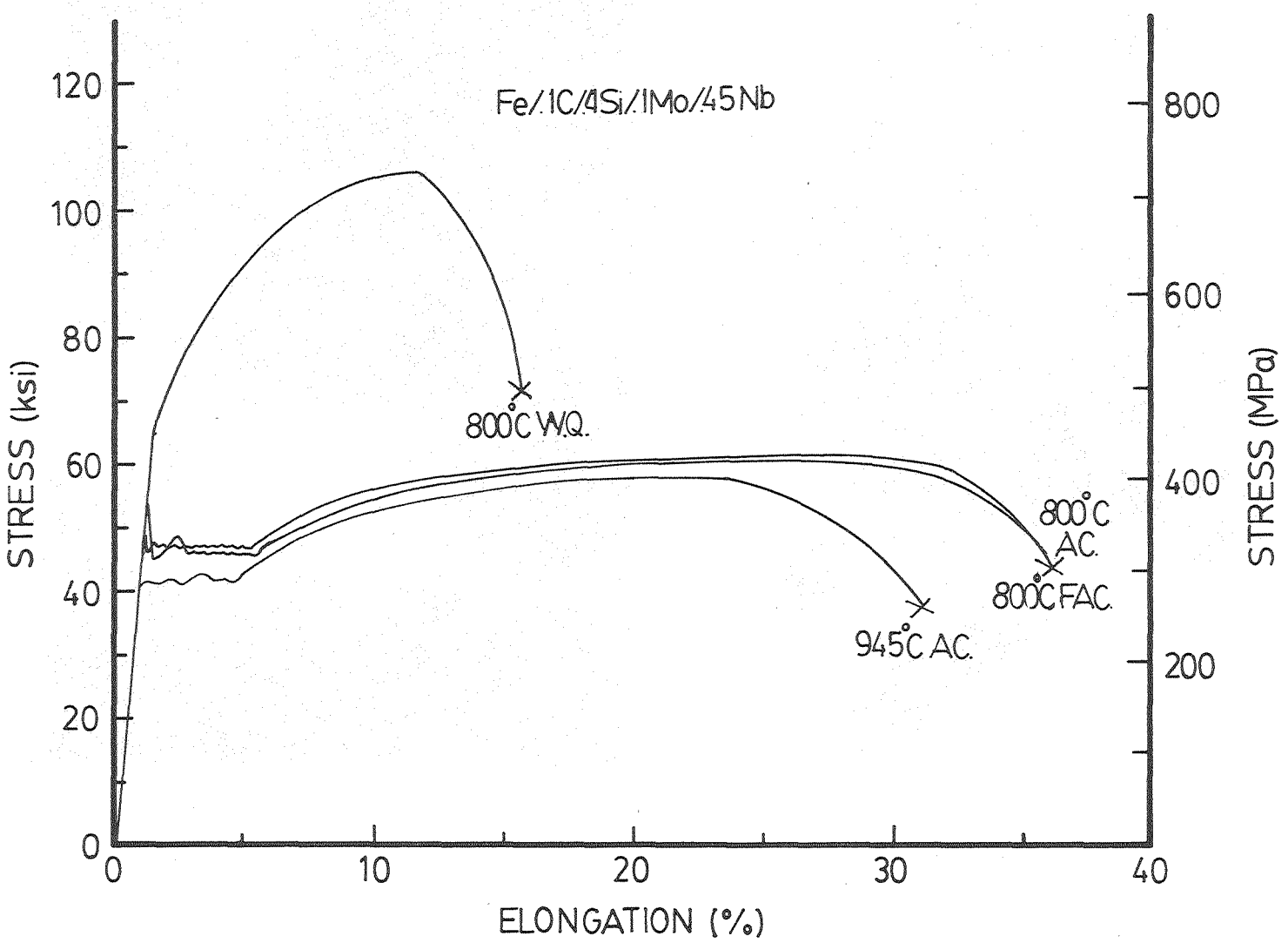

Fig. 22

XBL 8010-12572

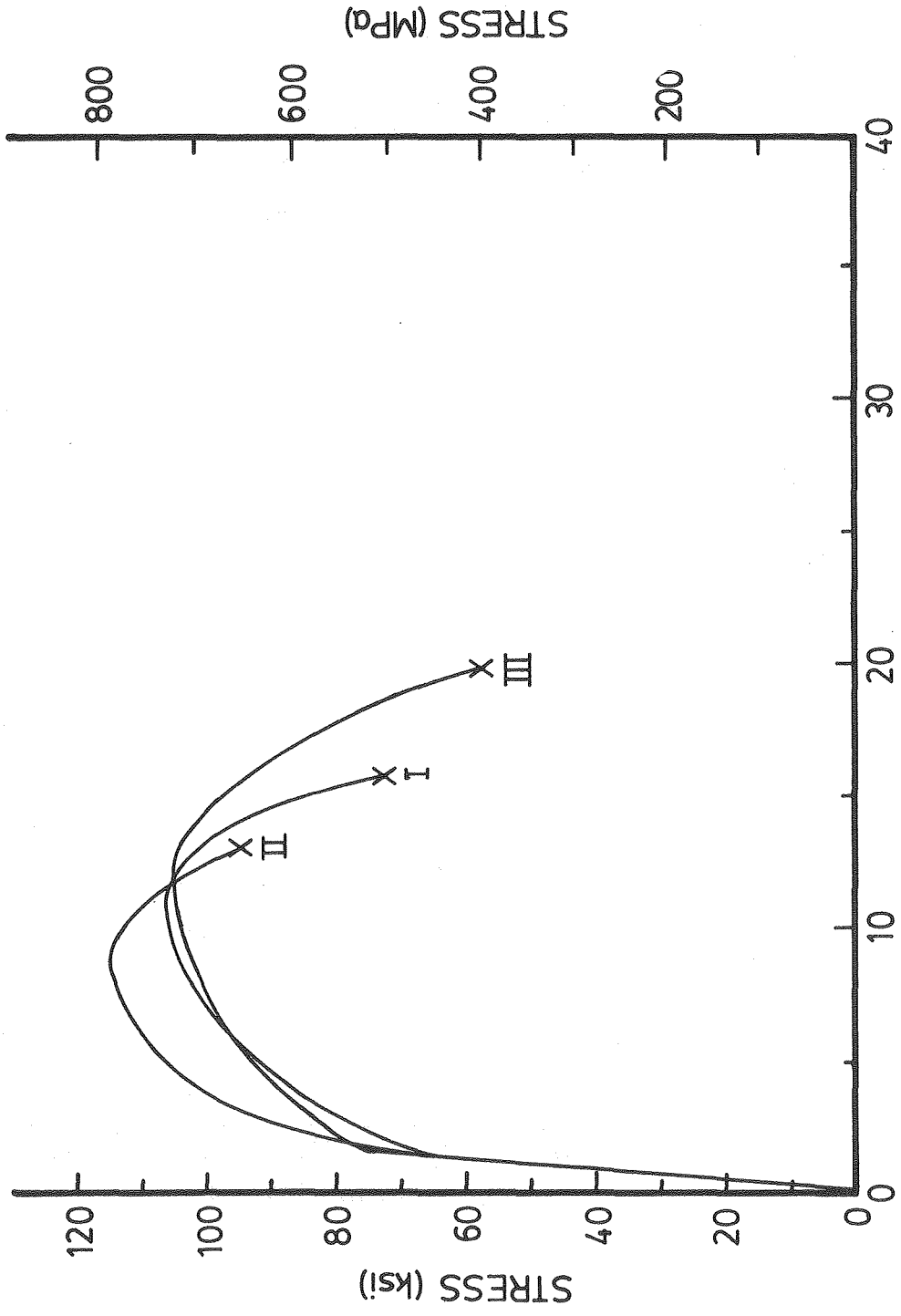

XBL 8010-6161

Fig. 23

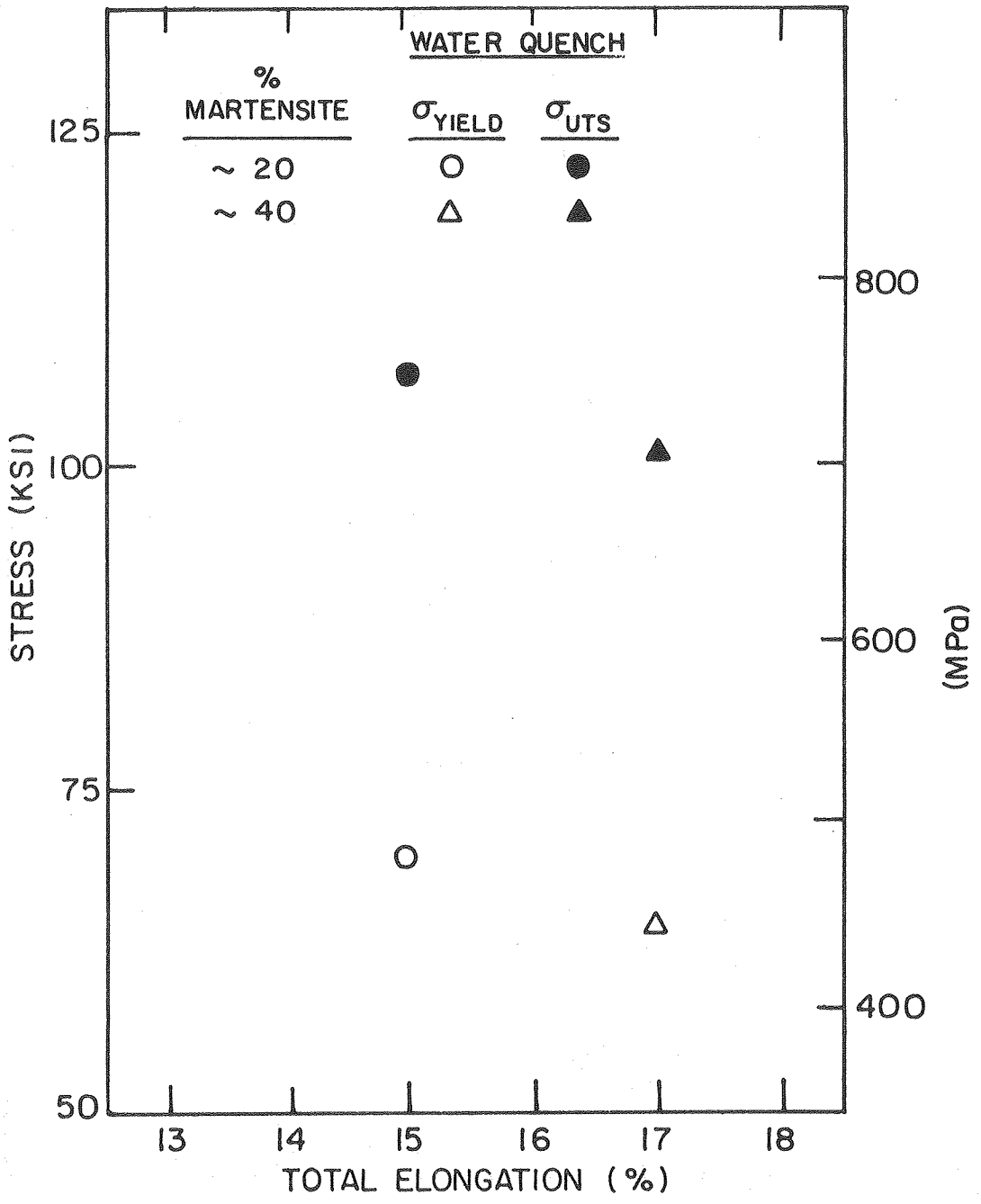

Fig. 24

XBL 8012-13433

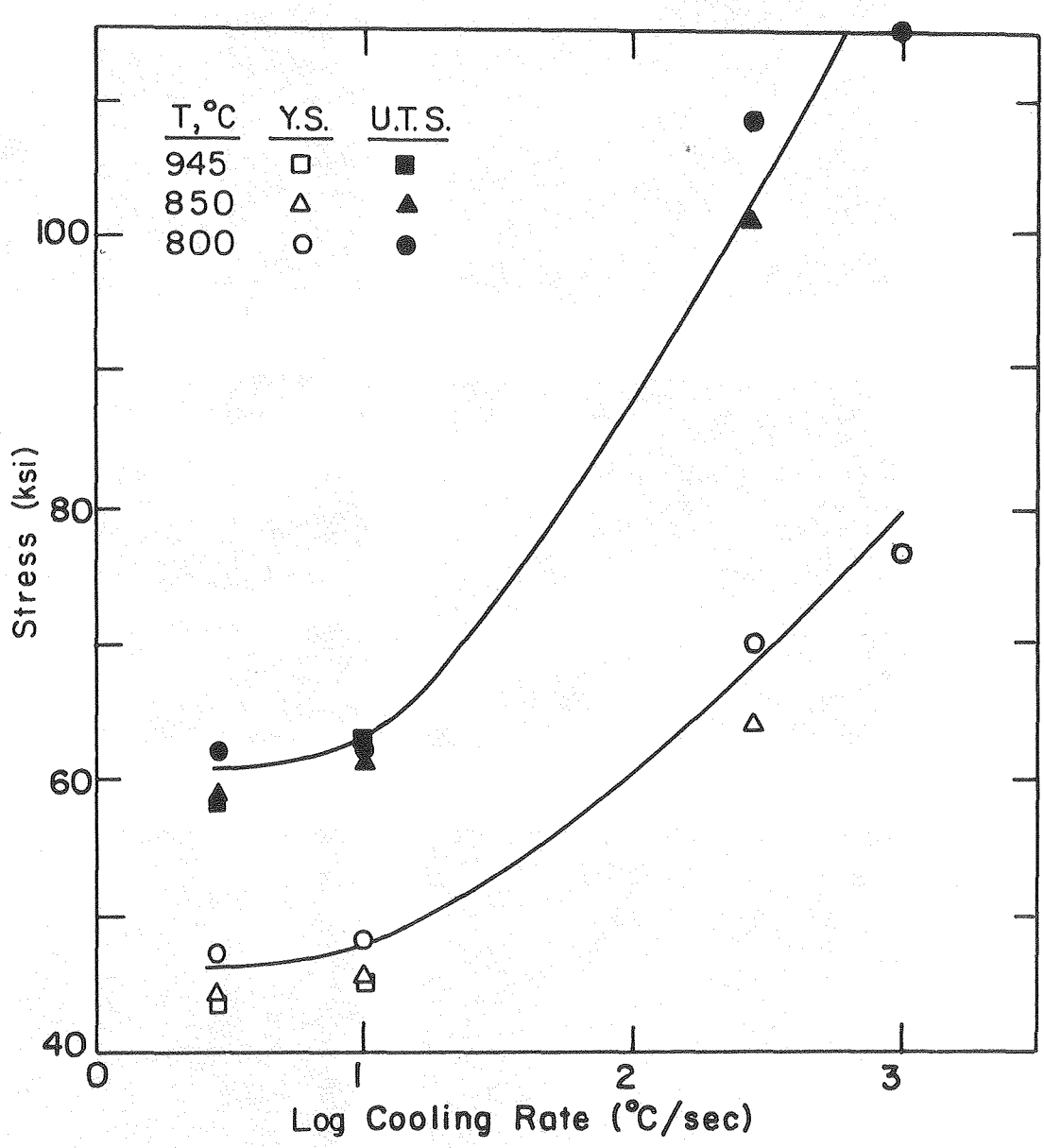

XBL 8010-6193

Fig. 25

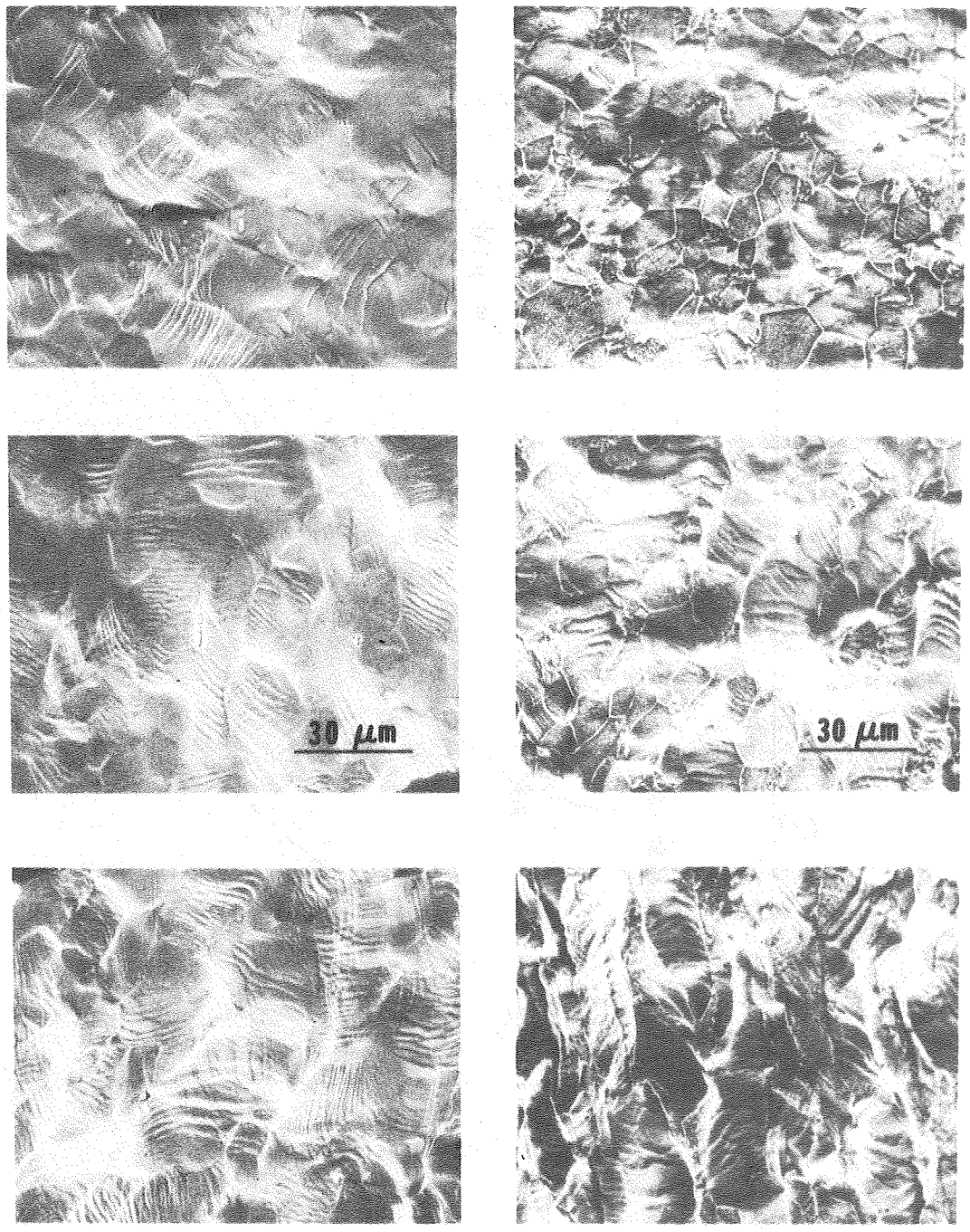

XBB 800-14030

Fig. 26

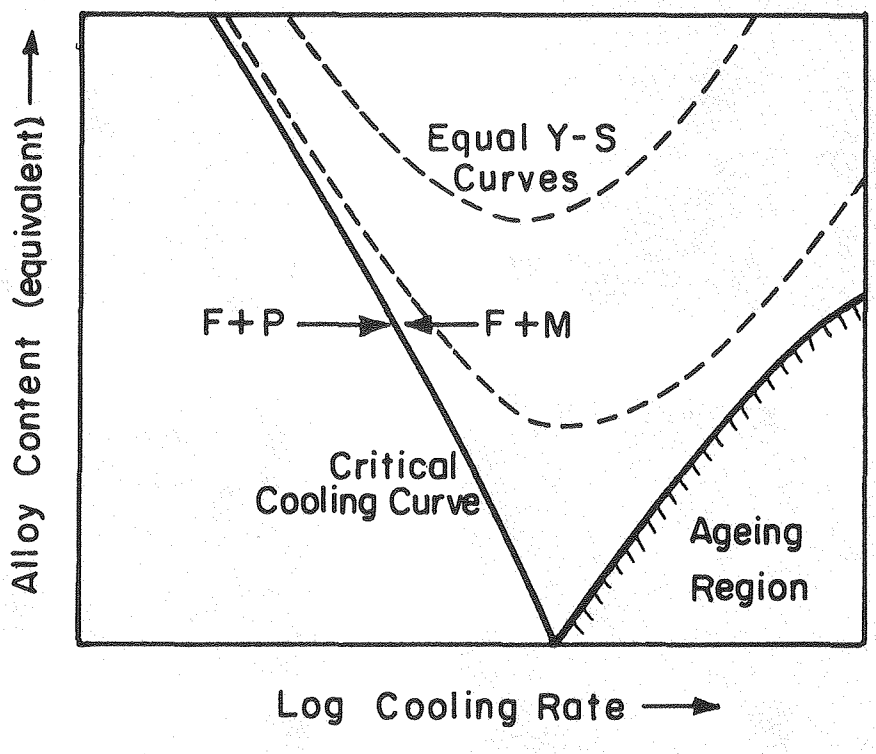

Fig. 27

XBL 8010-6194

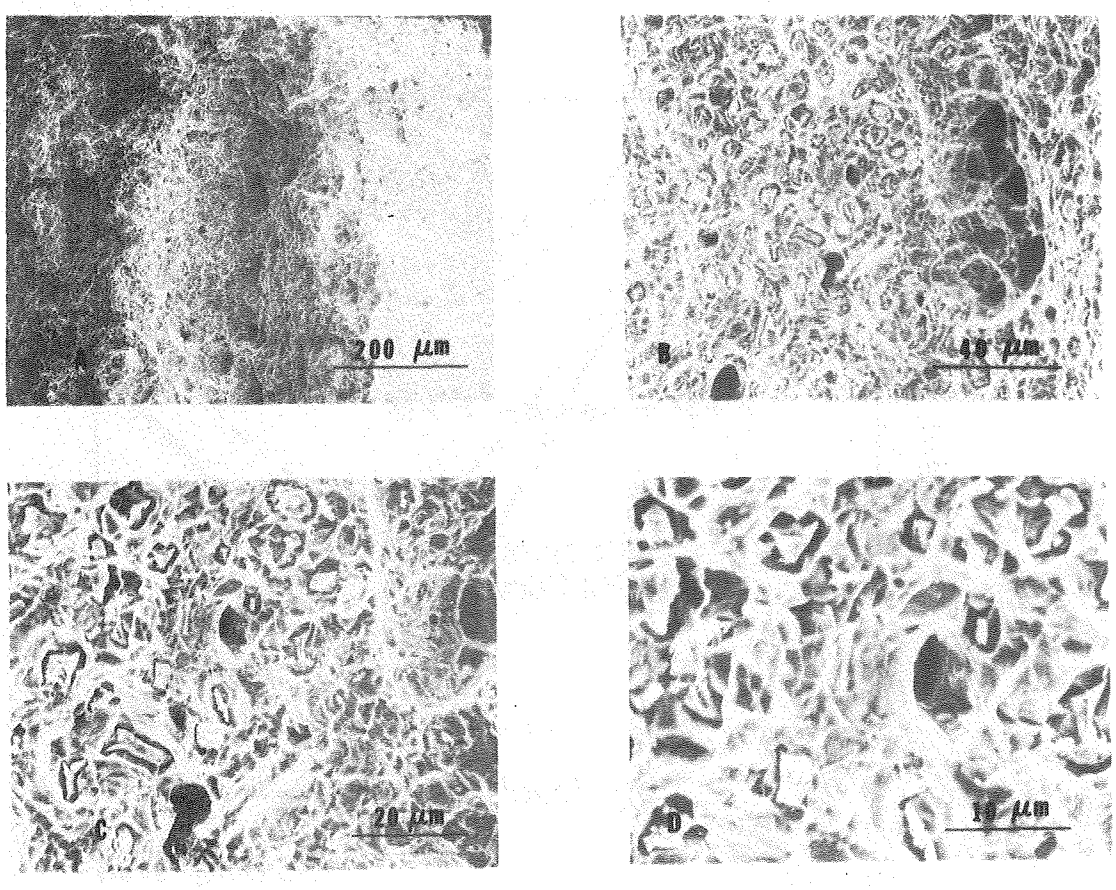

XBB 800-14491

Fig. 28

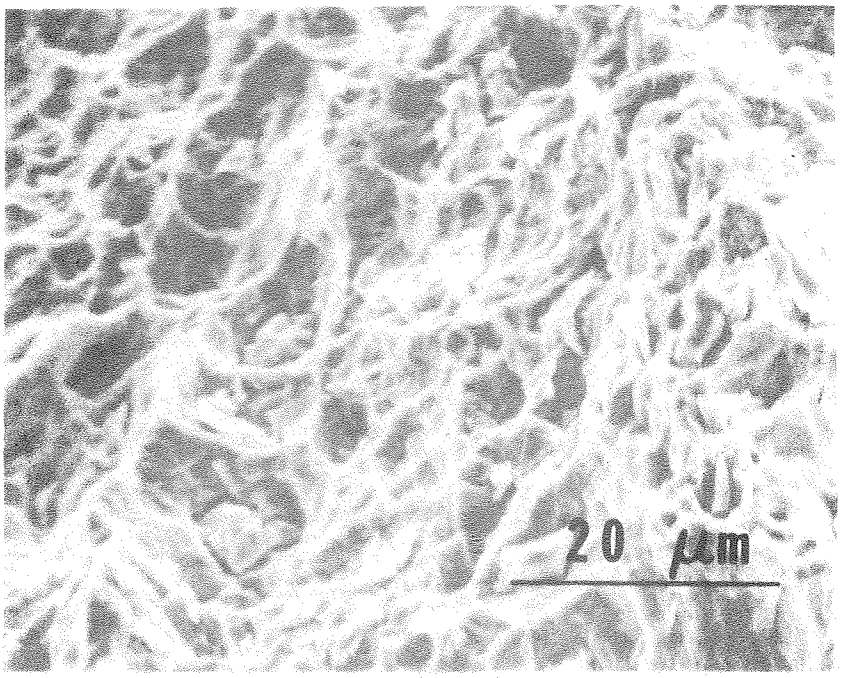

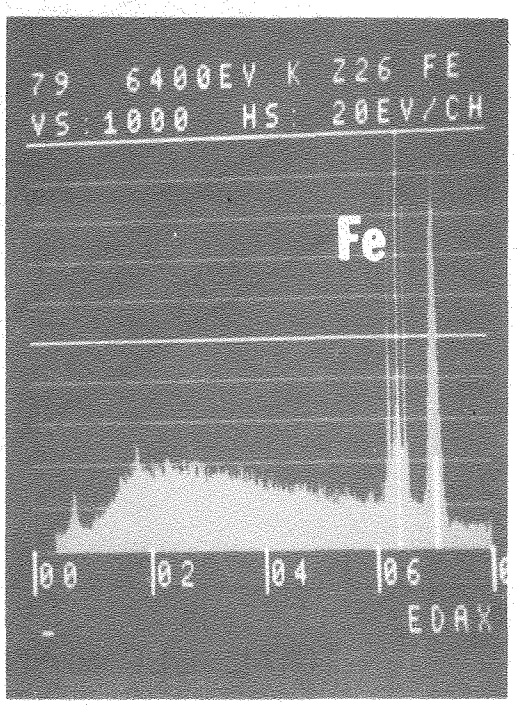

XBB 800-14037

Fig. 29

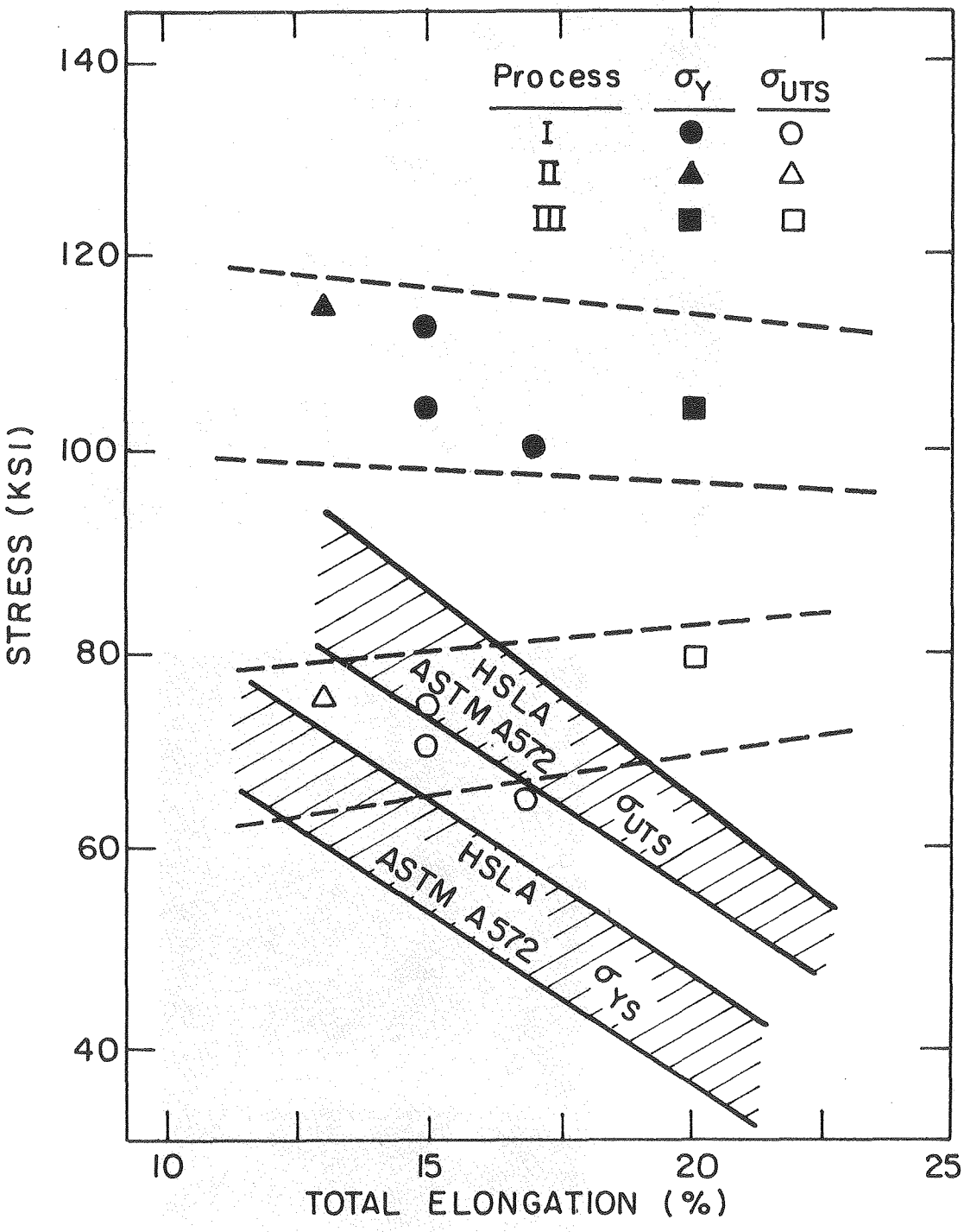

Fig. 30

XBL 812-5303